

Research Article

FE-Meshfree QUAD4 Element with Modified Radial Point Interpolation Function for Structural Dynamic Analysis

Hongjun Zhang , Guangsong Chen , Linfang Qian, and Jia Ma

School of Mechanical Engineering, Nanjing University of Science and Technology, Nanjing City 210094, China

Correspondence should be addressed to Guangsong Chen; cgsnjust@163.com

Received 3 August 2018; Revised 26 November 2018; Accepted 11 December 2018; Published 8 January 2019

Academic Editor: Marco Gherlone

Copyright © 2019 Hongjun Zhang et al. This is an open access article distributed under the Creative Commons Attribution License, which permits unrestricted use, distribution, and reproduction in any medium, provided the original work is properly cited.

The partition-of-unity method based on FE-Meshfree QUAD4 element synthesizes the respective advantages of meshfree and finite element methods by exploiting composite shape functions to obtain high-order global approximations. This method yields high accuracy and convergence rate without necessitating extra nodes or DOFs. In this study, the FE-Meshfree method is extended to the free and forced vibration analysis of two-dimensional solids. A modified radial point interpolation function without any supporting tuning parameters is applied to construct the composite shape functions. The governing equations of elastodynamic problem are transformed into a standard weak formulation and then discretized into time-dependent equations which are solved via Bathe time integration scheme to conduct the forced vibration analysis. Several numerical test problems are solved and compared against previously published numerical solutions. Results show that the proposed FE-Meshfree QUAD4 element owns greater tolerance for mesh distortion and provides more accurate solutions.

1. Introduction

Analysis of structural dynamics problems is a crucial step in many engineering applications. However, existing analytical methods are limited, as it is very challenging to find an exact solution to a class of dynamic problems. In addition, such solutions are reachable only with simple geometrical configurations and boundary conditions. Accordingly, numerical methods have emerged as an alternative approach to gain approximate solutions, which now represent the most widely used computational engineering tools.

Finite element method (FEM), serving as one of the most popular numerical approaches, is employed to analyze the structural vibration characteristics [1–3]. It is accurate, convenient, and flexible and has been successfully applied in solid mechanics, fluid mechanics, heat transfer, and other fields. However, the gradient of lower-order elements often exhibits discontinuity at element boundaries and nodes, accordingly rendering it unreliable in certain situations. Some isoparametric elements are also

highly sensitive to mesh distortion, which decreases the accuracy of some FEM-based solutions [4, 5]. Meshfree methods only employ nodes to discretize the problem domain and therefore are immune to mesh distortion problems. They are suitable for solving complex practical problems such as large deformation, fracture propagation simulation, and impact-induced failure [6–15]. However, there exist important drawbacks for meshfree methods, such as the essential boundary condition implementation handicap, high computational cost, and complex trial function construction process, thereby giving rise to several hybrid schemes to enhance the applicability of meshfree methods. Liu et al. [16], for example, developed the smoothed finite element method (SFEM) by combining the existing FEM technology and the strain-smoothing technique of meshfree methodology [17]. In SFEM, the strain is smoothed based on nodes or the edges of elements. SFEM provides an upper bound solution for problems of solid mechanics making it complementary to FEM. Other hybrid methods have also been proposed over the past decades [18–27].

Another common and extensively studied hybrid method is the partition-of-unity method (PUM) [28, 29]. The PUM can also be utilized to develop HP-clouds [30], generalized finite element method (GFEM) [31], particle-PUM [32], numerical manifold method [33], and extended FEM [34, 35]. PUM also serves as a convenient approach to construct the higher-order global approximations without adding external nodes, thereby achieving higher accuracy and convergence rate than other methods. However, PUM has a serious disadvantage known as the “linear dependence” (LD) problem [36], wherein the global stiffness matrix remains singular after applying the basic boundary condition to eliminate the rigid body displacement. LD occurs when both the PUM functions and the local approximation functions are taken as explicit polynomials. Tian et al. [37] conducts a comprehensive review about some effective approaches to eliminate the LD problem. Recently, a new family of elements called “FE-Meshfree” elements based on the PUM has been developed as a combination of the respective strengths of meshfree and FEM techniques such as the PU-based FE-Meshfree QUAD4 element by Rajendran et al. [38, 39], FE-Meshfree RRIA3 element by Xu [36], FE-Meshfree elements with continuous nodal stress for 2D and 3D problems by Tang and Yang [40–42], FE-Meshfree QUAD4 element with radial-polynomial basis functions by Xu [43], PU-based FE-Meshfree QUAD4 and triangular with continuous nodal stress by Yang [44, 45], and others [46, 47]. FE-Meshfree features the composite shape functions, which are constructed by combining the meshfree and finite element shape functions. The shape functions of FE-Meshfree elements possess the much desired Kronecker delta property, which is crucial in the implementation process of essential boundary conditions under FEM, interelement compatibility properties, and all the completeness properties that are necessary to ensure the reproducibility of not only the linear polynomial terms but also the higher-order terms in the local approximation. FE-Meshfree elements, as opposed to FEM elements, inherit some advantages, like better accuracy, higher convergence rate, and greater robustness to mesh distortion. FE-Meshfree elements are also free from the LD problem which exists in many of the PUM-based finite elements. PU-based FE-Meshfree method has already been applied successfully within statics, free vibration [48, 49], forced vibration [50], geometric nonlinearity [51, 52], acoustic engineering [53], and other fields.

In the present study, the FE-Meshfree method with modified radial point interpolation function is to be applied in the free and forced vibration analysis of two-dimensional solids. The rest of this paper is organized as follows. Section 2 briefly reviews the formulation of the composite shape function and the modified radial point interpolation function. This is followed by the equations for free and forced vibration analysis in Section 3. Section 4 is devoted to the numerical tests, in which the convergence and accuracy of the proposed method is verified. Finally, conclusions are drawn in Section 5.

2. Composite Shape Functions Based on Modified Radial Based Function

2.1. Composite Shape Function. Regarding the composite shape functions for the FE-Meshfree QUAD4 element, constituted by the combination of radial-polynomial basis functions proposed by Xu [43], the displacement interpolation in j -th element e_j can be written as follows:

$$u(\mathbf{x}) = \sum_{i=1}^4 N_i(\mathbf{x})u_i(\mathbf{x}), \quad (1)$$

where $N_i(\mathbf{x})$ ($i = 1, 2, \dots, 4$) are isoparametric shape functions used in the classic QUAD4 element and $u_i(\mathbf{x})$ denotes the nodal displacement function vector which can be constructed by the nodes in the node support domain Ω_i which is defined by the element including node i . As shown in Figure 1, the node support domain Ω_1 for node $i = 1$ is marked by a dashed line, which includes nodes $\{1, 2, 3, 4, 5, 6, 7, 8, 9\}$. Regarding the unknown nodal displacement functions, they can be interpolated by the polynomial basis function $p_z(\mathbf{x})$ and radial basis function $r_j(\mathbf{x})$, which can be expressed as follows:

$$u_i(\mathbf{x}) = \sum_{j=1}^n r_j(\mathbf{x})a_j + \sum_{z=1}^m p_z(\mathbf{x})b_z = \mathbf{r}^T(\mathbf{x})\mathbf{a} + \mathbf{p}^T(\mathbf{x})\mathbf{b}. \quad (2)$$

In the above, m is the number of polynomial terms and n denotes the number of nodes in the node support domain Ω_i .

The vectors \mathbf{a} and \mathbf{b} in equation (2) are vectors yet to be determined. $\mathbf{p}(\mathbf{x})$ and $\mathbf{r}(\mathbf{x})$ denote the corresponding polynomial and radial basis functions, respectively. If we consider three respective terms for 2D problems, $\mathbf{p}(\mathbf{x})$ can be written as follows:

$$\mathbf{p}(\mathbf{x}) = [1 \ x \ y]^T. \quad (3)$$

The radial basis function vector $\mathbf{r}(\mathbf{x})$ is expressed as

$$\mathbf{r}(\mathbf{x}) = [r_1(d_1) \ r_2(d_2) \ \dots \ r_k(d_k) \ \dots \ r_n(x, y)]^T, \quad (4)$$

where $r_k(d_k)$ is the function of distance d_k , which denotes the space distance between the selected interpolation point \mathbf{x} and a node \mathbf{x}_k . Also for the 2D problem, d_k can be expressed as

$$d_k = d_k(x, y) = \sqrt{(x - x_k)^2 + (y - y_k)^2}. \quad (5)$$

Enforcing equation (2) to pass through all the nodes in the nodal support domain yields the following equation:

$$\mathbf{u}_i = \mathbf{R}\mathbf{a} + \mathbf{P}\mathbf{b}, \quad (6)$$

where \mathbf{u}_i is a nodal displacement vector of all the nodes in the nodal support domain and \mathbf{a} and \mathbf{b} are, respectively, the vector of unknown coefficients for radial basis functions and polynomial basis functions:

$$\begin{aligned} \mathbf{a}^T &= \{a_1 \ a_2 \ \dots \ a_n\}, \\ \mathbf{b}^T &= \{b_1 \ b_2 \ \dots \ b_m\}. \end{aligned} \quad (7)$$

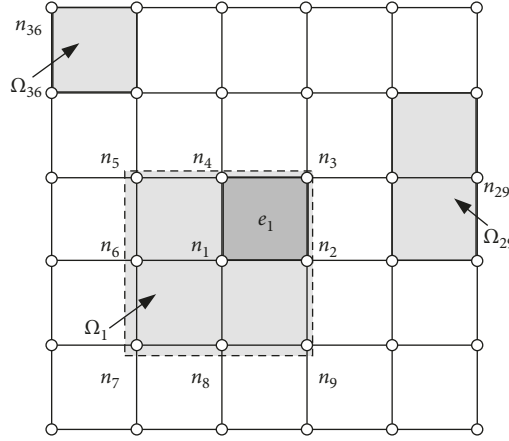


FIGURE 1: Nodal support domain.

The related matrices \mathbf{R} and \mathbf{P} are

$$\mathbf{R} = \begin{bmatrix} r_1(x_1, y_1) & r_2(x_1, y_1) & \cdots & r_n(x_1, y_1) \\ r_1(x_2, y_2) & r_2(x_2, y_2) & \cdots & r_n(x_2, y_2) \\ \vdots & \vdots & \ddots & \vdots \\ r_1(x_n, y_n) & r_2(x_n, y_n) & \cdots & r_n(x_n, y_n) \end{bmatrix}, \quad (8)$$

$$\mathbf{P} = \begin{bmatrix} p_1(x_1, y_1) & p_2(x_1, y_1) & \cdots & p_m(x_1, y_1) \\ p_1(x_2, y_2) & p_2(x_2, y_2) & \cdots & p_m(x_2, y_2) \\ \vdots & \vdots & \ddots & \vdots \\ p_1(x_n, y_n) & p_2(x_n, y_n) & \cdots & p_m(x_n, y_n) \end{bmatrix}.$$

The following constraint condition can be imposed to guarantee a unique displacement approximation as follows [54]:

$$\mathbf{P}^T \mathbf{a} = \mathbf{0}. \quad (9)$$

From equation (6), we can obtain:

$$\mathbf{a} = \mathbf{R}^{-1} \mathbf{u}_i - \mathbf{R}^{-1} \mathbf{P} \mathbf{b}. \quad (10)$$

Substituting equation (10) into equation (9), the vector \mathbf{b} can be solved:

$$\mathbf{b} = \mathbf{S}_b \mathbf{u}_i, \quad (11)$$

$$\mathbf{S}_b = [\mathbf{P}^T \mathbf{R}^{-1} \mathbf{P}]^{-1} \mathbf{P}^T \mathbf{R}^{-1}. \quad (12)$$

Substituting equation (11) into equation (10), the vector \mathbf{a} can be obtained:

$$\mathbf{a} = \mathbf{S}_a \mathbf{u}_i, \quad (13)$$

$$\mathbf{S}_a = \mathbf{R}^{-1} [\mathbf{I} - \mathbf{P} \mathbf{S}_b] = \mathbf{R}^{-1} - \mathbf{R}^{-1} \mathbf{P} \mathbf{S}_b. \quad (14)$$

Eventually the nodal displacement function can be expressed by substituting equations (11) and (13) into equation (2):

$$u_i(x, y) = \Phi_i \mathbf{u}_i, \quad i = 1, 2, 3, 4, \quad (15)$$

$$\Phi_i = \mathbf{r}^T(x, y) \mathbf{S}_a + \mathbf{p}^T(x, y) \mathbf{S}_b,$$

where

$$\Phi_i = [\Phi_1^i \quad \Phi_2^i \quad \cdots \quad \Phi_N^i], \quad (16)$$

$$\mathbf{u}_i = [u_1 \quad u_2 \quad \cdots \quad u_N]^T.$$

The arrays Φ_i , $i = 1, 2, 3, 4$ are to be assembled into a matrix Φ , in which L is the number of nodes in the j -th element support domain Ω^j which is defined by the element including nodes in element j . As shown in Figure 2, the element support domain $\Omega^1 = \Omega_1 \cup \Omega_2 \cup \Omega_3 \cup \Omega_4 = \{1, 2, 3, 4, 5, 6, 7, 8, 9, 10, 11, 12, 13, 14, 15, 16\}$ for element $j = 1$ is marked by a dot dash line.

Substituting equations (10) and (11) into equation (1) allows us to rewrite the element displacement field as follows:

$$u(\mathbf{x}) = \mathbf{N}_{1 \times 4} \left(\Phi_{4 \times L} \mathbf{u}_{L \times 1} \right) = \left(\mathbf{N} \Phi \right)_{1 \times 4 \times L} \mathbf{u}_{L \times 1} = \Psi_{1 \times L} \mathbf{u}_{L \times 1}. \quad (17)$$

In the above, \mathbf{u} denotes the x -direction displacement of all the nodes in an element support domain Ω^e , and the composite shape function array, Ψ , can be represented as

$$\Psi_{1 \times L} = [\psi_1, \psi_2, \cdots, \psi_L] = \mathbf{N}_{1 \times 4} \Phi_{4 \times L}. \quad (18)$$

Similarly, the element displacement field in y -direction is written as follows:

$$v(\mathbf{x}) = \Psi_{1 \times L} \mathbf{v}_{L \times 1}, \quad (19)$$

where \mathbf{v} denotes the y -direction displacements of all nodes in Ω^e .

The Cartesian derivatives of shape function are obtained by

$$\Psi_{,x} = [\psi_{1,x} \quad \psi_{2,x} \quad \cdots \quad \psi_{L,x}] = \mathbf{N}_{,x} \Phi + \mathbf{N} \Phi_{,x}, \quad (20)$$

$$\Psi_{,y} = [\psi_{1,y} \quad \psi_{2,y} \quad \cdots \quad \psi_{L,y}] = \mathbf{N}_{,y} \Phi + \mathbf{N} \Phi_{,y}.$$

The composite shape function Ψ is characterized by the Kronecker delta property, interelement compatibility property, and higher-order completeness properties, i.e., the

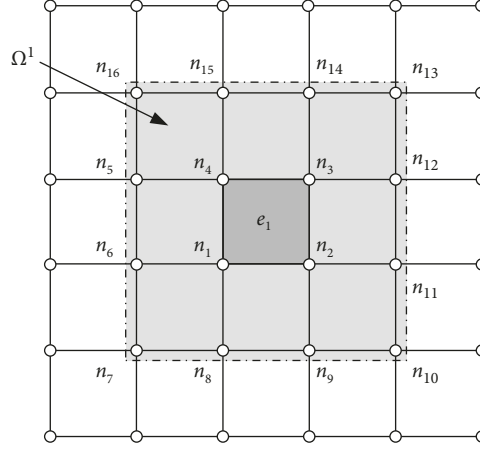


FIGURE 2: Element support domain.

reproducibility of all the Cartesian terms appearing under the assumed basis of equation (1).

2.2. Modified Radial Based Function. During the numerical analysis process, many specific radial basis functions are used in radial point interpolation method (RPIM) to ensure favorable performances. The typical radial basis functions, usually employed in engineering problems, are tabulated in Table 1. However, the tuning parameters show significant influences on the quality of the basis function during the shape functions construction process to achieve a smooth solution. So far, the optimal values of the shape parameters are still being explored and remain questionable.

In this study, we used the modified basis function proposed by Do [55] to construct the composite shape functions without any supporting tuning parameters. The radial basis function can be taken as a compactly supported form:

$$r_k(\mathbf{x}) = s(\bar{\mathbf{d}}_k)M(\bar{\mathbf{d}}_k), \quad (21)$$

$$\bar{\mathbf{d}}_k = \frac{d_k}{d_s}.$$

In the above, $s(\bar{\mathbf{d}}_k)$ denotes a compactly supported function, $M(\bar{\mathbf{d}}_k)$ represents a radial basis function, and d_s is the size of the support domain. Generally, $s(\bar{\mathbf{d}}_k)$ can be chosen as a Heaviside step function, if $\bar{\mathbf{d}}_k \leq 1$, $s(\bar{\mathbf{d}}_k) = 1$, otherwise, $s(\bar{\mathbf{d}}_k) = 0$. However, as the nodal support domain and the corresponding nodes have been defined, $s(\bar{\mathbf{d}}_k)$ does not need to be used, and equation (21) can be rewritten as

$$r_k(\mathbf{x}) = M(\bar{\mathbf{d}}_k), \quad (22)$$

$$\bar{\mathbf{d}}_k = \frac{d_k}{d_s}.$$

The following radial basis function in a compactly supported form based on the original kernel function of the quartic spline (QS) [6] is applied:

TABLE 1: Typical radial basis functions.

Name	Expression	Parameters
Gaussian (exp)	$r_j(x, y) = \exp[-b(d_j/d_c)^2]$	b
Multiquadrics (MQ)	$r_j(x, y) = [d_j^2 + (bd_c)^2]^q$	b, q
Inverse multiquadrics (IMQ)	$r_j(x, y) = 1/[d_j^2 + (bd_c)^2]^q$	b, q

$$M(\bar{\mathbf{d}}_k) = 1 - 6 \times (\theta \bar{\mathbf{d}}_k)^2 + 8 \times (\theta \bar{\mathbf{d}}_k)^3 - 3 \times (\theta \bar{\mathbf{d}}_k)^4. \quad (23)$$

The correlation parameter θ can be set to any value due to the normalized distance, which is demonstrated by numerical examples below, and we revisit this in Section 4.3.1. The circular or rectangular support domain can be applied in the meshfree method, but in this work, the node support domain is inherently suitable as a support domain and its equivalent radius is defined as follows:

$$d_s = \kappa d_c, \quad (24)$$

where κ is the scale factor and d_c is a characteristic length related to the nodal distance, which can be estimated as the average distance between a group of nodes in the support domain. d_c is determined as follows for the irregular nodal distribution [56]:

$$d_c = \frac{\sqrt{A_s}}{\sqrt{n_{A_s} - 1}}, \quad (25)$$

where A_s denotes the area of the nodal support domain and n_{A_s} is the corresponding number of nodes in the nodal support domain.

Substituting equation (24) into equation (23), equation (23) can be rewritten as

$$M(d_k) = 1 - 6 \times \left(\frac{\theta}{\kappa} \frac{d_k}{d_c}\right)^2 + 8 \times \left(\frac{\theta}{\kappa} \frac{d_k}{d_c}\right)^3 - 3 \times \left(\frac{\theta}{\kappa} \frac{d_k}{d_c}\right)^4. \quad (26)$$

From equation (26), θ/κ can be regarded as one variable; therefore, $\kappa = 1$ can be adopted in the presented formulation.

3. Structural Dynamic Analysis

3.1. Discrete Governing Equations. Here, we consider a deformable body Ω subjected to body force \mathbf{f} , traction \mathbf{t} on boundary Γ_t , and displacement boundary conditions $\mathbf{u} = \bar{\mathbf{u}}$ on Γ_u , where $\Gamma = \Gamma_t \cup \Gamma_u$, $\Gamma_t \cap \Gamma_u = \emptyset$. The virtual weak form of the dynamic equation can be expressed as

$$\int_{\Omega} \delta \boldsymbol{\varepsilon}^T \boldsymbol{\sigma} d\Omega - \int_{\Omega} \delta \mathbf{u}^T [\mathbf{f} - \rho \ddot{\mathbf{u}} - c \dot{\mathbf{u}}] d\Omega - \int_{\Gamma_t} \delta \mathbf{u}^T \mathbf{t} d\Gamma = 0, \quad (27)$$

where ρ and c are the density and the coefficient of damping. $\boldsymbol{\varepsilon}$ and $\boldsymbol{\sigma}$ denote the strain and stress in the element. As the spatial discretization procedure in the FEM, the virtual displacements and strains within element can be expressed as

$$\mathbf{u} = \sum_I \mathbf{N}_I \mathbf{d}_I, \quad (28)$$

$$\delta \mathbf{u} = \sum_I \mathbf{N}_I \delta \mathbf{d}_I,$$

$$\boldsymbol{\varepsilon} = \sum_I \mathbf{B}_I \mathbf{d}_I, \quad (29)$$

$$\delta \boldsymbol{\varepsilon} = \sum_I \mathbf{B}_I \delta \mathbf{d}_I,$$

where $\mathbf{d}_I = [u_I \ v_I]^T$ is the nodal displacement vector and \mathbf{B} represents the standard displacement gradient matrix. For 2D problems, it can be determined as follows:

$$\mathbf{B}_I = \nabla_S \mathbf{N}_I(x) = \begin{bmatrix} N_{I,x} & 0 \\ 0 & N_{I,y} \\ N_{I,y} & N_{I,x} \end{bmatrix}. \quad (30)$$

The stress can be obtained by the following constitutive relation:

$$\boldsymbol{\sigma} = \mathbf{D} \boldsymbol{\varepsilon}, \quad (31)$$

where \mathbf{D} is the matrix of the elastic constants of the material.

Substituting equations (28) and (29) into equation (27) yields

$$\int_{\Omega} \delta \mathbf{d}^T \mathbf{B}^T \boldsymbol{\sigma} d\Omega - \int_{\Omega} \delta \mathbf{d}^T \mathbf{N}^T [\mathbf{f} - \rho \ddot{\mathbf{u}} - c \dot{\mathbf{u}}] d\Omega - \int_{\Gamma_t} \delta \mathbf{d}^T \mathbf{N}^T \mathbf{t} d\Gamma = 0. \quad (32)$$

According to the principle of virtual work, the discrete governing equation can be expressed as

$$\int_{\Omega} \mathbf{B}^T \boldsymbol{\sigma} d\Omega - \int_{\Omega} \mathbf{N}^T [\mathbf{f} - \rho \ddot{\mathbf{u}} - c \dot{\mathbf{u}}] d\Omega - \int_{\Gamma_t} \mathbf{N}^T \mathbf{t} d\Gamma = 0, \quad (33)$$

or

$$\mathbf{M} \ddot{\mathbf{d}} + \mathbf{C} \dot{\mathbf{d}} + \mathbf{K} \mathbf{d} = \mathbf{f}^{\text{ext}}, \quad (34)$$

in which

$$\begin{aligned} \mathbf{f}^{\text{ext}} &= \int_{\Omega} \mathbf{N}^T \mathbf{f} d\Omega + \int_{\Gamma_t} \mathbf{N}^T \mathbf{t} d\Gamma, \\ \mathbf{M} &= \int_{\Omega} \mathbf{N}^T \rho \mathbf{N} d\Omega, \\ \mathbf{K} &= \int_{\Omega} \mathbf{B}^T \mathbf{D} \mathbf{B} d\Omega, \\ \mathbf{C} &= \int_{\Omega} \mathbf{N}^T c \mathbf{N} d\Omega. \end{aligned} \quad (35)$$

3.2. Free Vibration Analysis. The damping and external forces are not taken into account during free vibration analysis. Accordingly, equation (34) can be reduced to a system of homogeneous equations [1]:

$$\mathbf{M} \ddot{\mathbf{d}} + \mathbf{K} \mathbf{d} = 0. \quad (36)$$

A general solution to this system is

$$\mathbf{d} = \bar{\mathbf{d}} \exp(i\omega t), \quad (37)$$

where i denotes the imaginary unit, t is time, $\bar{\mathbf{d}}$ indicates the eigenvector, and ω is the natural frequency. Substituting equation (37) into equation (36) leads to the following eigenvalue equation for natural frequency ω :

$$(-\omega^2 \mathbf{M} + \mathbf{K}) \bar{\mathbf{d}} = 0. \quad (38)$$

The natural frequencies and corresponding mode shapes of a given structure are often referred to as the dynamic characteristics of the structure.

3.3. Forced Vibration Analysis. In the forced vibration analysis, equation (34) is a function of both space and time. For simplicity, a constant damping matrix \mathbf{C} which is assumed to be a linear combination of \mathbf{M} and \mathbf{K} can be utilized as

$$\mathbf{C} = \alpha \mathbf{M} + \beta \mathbf{K}, \quad (39)$$

where α and β are the Rayleigh damping coefficients.

There exist many numerical integration methods, such as Newmark method, Wilson method, generalized- α method [57], and so on. Here, the Bathe method, as briefly discussed as below [58–60], is used in this work. Two equal substeps are included in the complete time step h in Bathe method. In the first substep, the following equations are obtained by using the trapezoidal rule:

$$\begin{cases} \dot{\mathbf{d}}_{t+h/2} = \frac{4}{h} (\mathbf{d}_{t+h/2} - \mathbf{d}_t) - \dot{\mathbf{d}}_t, \\ \ddot{\mathbf{d}}_{t+h/2} = \frac{16}{h^2} \left(\mathbf{d}_{t+h/2} - \mathbf{d}_t - \frac{h}{2} \dot{\mathbf{d}}_t \right) - \ddot{\mathbf{d}}_t. \end{cases} \quad (40)$$

Substituting equation (40) into equation (33) yields the following algebraic equation:

$$\begin{aligned} & \left(\frac{16}{h^2} \mathbf{M} + \frac{4}{h} \mathbf{C} + \mathbf{K} \right) \mathbf{d}_{t+h/2} - \mathbf{M} \left(\frac{16}{h^2} \mathbf{d}_t + \frac{8}{h} \dot{\mathbf{d}}_t + \ddot{\mathbf{d}}_t \right) \\ & - \mathbf{C} \left(\frac{4}{h} \mathbf{d}_t + \dot{\mathbf{d}}_t \right) = \mathbf{f}^{\text{ext}}. \end{aligned} \quad (41)$$

In the second substep, the following equations are expressed by the three-point Euler backward method:

$$\begin{cases} \dot{\mathbf{d}}_{t+h} = \frac{1}{h} \mathbf{d}_t - \frac{4}{h} \mathbf{d}_{t+h/2} + \frac{3}{h} \mathbf{d}_{t+h}, \\ \ddot{\mathbf{d}}_{t+h} = \frac{1}{h} \dot{\mathbf{d}}_t - \frac{4}{h} \dot{\mathbf{d}}_{t+h/2} + \frac{3}{h} \dot{\mathbf{d}}_{t+h}. \end{cases} \quad (42)$$

Similarly, the control equation (34) at time $t+h$ can also be expressed as

$$\begin{aligned} & \left(\frac{9}{h^2} \mathbf{M} + \frac{3}{h} \mathbf{C} + \mathbf{K} \right) \mathbf{d}_{t+h} + \mathbf{M} \left(\frac{1}{h} \dot{\mathbf{d}}_t - \frac{4}{h} \dot{\mathbf{d}}_{t+h/2} + \frac{3}{h^2} \mathbf{d}_t - \frac{12}{h^2} \mathbf{d}_{t+h/2} \right) \\ & + \mathbf{C} \left(\frac{1}{h} \mathbf{d}_t - \frac{4}{h} \mathbf{d}_{t+h/2} \right) = \mathbf{Q}. \end{aligned} \quad (43)$$

Once $\mathbf{d}_{t+h/2}$ and \mathbf{d}_{t+h} is solved by equations (41) and (43), $\dot{\mathbf{d}}_{t+h/2}$, $\ddot{\mathbf{d}}_{t+h/2}$, $\dot{\mathbf{d}}_{t+h}$, and $\ddot{\mathbf{d}}_{t+h}$ can be obtained via equations (40) and (42).

4. Numerical Examples

To evaluate the accuracy of the method, the following displacement error norm and the strain energy norm are defined:

$$\begin{aligned} e_d &= \sqrt{\frac{\sum_{i=1}^{N_d} (u_i^{\text{exact}} - u_i^{\text{num}})^2}{\sum_{i=1}^{N_d} (u_i^{\text{exact}})^2}}, \\ e_e &= \frac{|E_{\text{num}} - E_{\text{exact}}|}{E_{\text{exact}}}, \end{aligned} \quad (44)$$

where superscript “exact” denotes the exact value of the problem, “num” denotes result solved by numerical solutions, and N_d is the number of total field nodes.

The strain energy of the numerical solution E_{num} and the total strain energy of the exact solution E_{exact} are defined as follows:

$$\begin{aligned} E_{\text{num}} &= \frac{1}{2} \mathbf{u}^T \mathbf{K} \mathbf{u}, \\ E_{\text{exact}} &= \frac{1}{2} \sum_{i=1}^{N_e} \int_{\Omega_i} \boldsymbol{\varepsilon}_i^T \mathbf{D} \boldsymbol{\varepsilon}_i d\Omega, \end{aligned} \quad (45)$$

where $\boldsymbol{\varepsilon}_i$ is the strain of the exact solution. In the actual computation on equation (45), we used a very fine mesh ($N_e \rightarrow \infty$) to calculate the “exact” strain energy E_{exact} .

In order to assess accuracy and convergence of each method for free vibration analysis, the relative error in the natural frequency is defined as follows:

$$R_e = \frac{f^{\text{num}} - f^{\text{ref}}}{f^{\text{ref}}}, \quad (46)$$

where the superscript “ref” represents the reference solution.

4.1. Example 1: Patch Test. Patch tests often serve as useful tools to evaluate the convergence of a numerical method based on the Galerkin weak form. Here, we use the generalized patch test introduced in [61], in which the coefficients of polynomial are not specifically predefined. The patch test is regarded as pass in the case that the maximum eigenvalue of the resulted matrix tends to zero.

As listed in [62], for the patch test, we can obtain

$$\begin{aligned} u^{\text{ex}} &= \sum a_{ij} p_{ij}(\mathbf{x}) = \mathbf{p}(\mathbf{x}) \mathbf{a}, \\ p_{ij}(\mathbf{x}) &= x^i y^j, \quad i + j \leq m, \end{aligned} \quad (47)$$

where $\mathbf{p}(\mathbf{x})$ and \mathbf{a} represent the row vector of monomials and the corresponding vector of coefficients, respectively, and m denotes the arbitrary maximum order of the monomials. Regarding each of these monomials in equation (47) as separate exact solution, a set of M numerical solutions can be obtained as

$$u_n^{\text{ex}} = p_n(\mathbf{x}), \quad n = 1, 2, \dots, M, \quad M = \frac{(m+1)(m+2)}{2}. \quad (48)$$

For the distributed nodes in the patch domain, a pointwise error vector can be evaluated as

$$\mathbf{e}_n = \mathbf{U}_n^{\text{ex}} - \mathbf{U}_n, \quad n = 1, 2, \dots, M, \quad (49)$$

where \mathbf{U}_n^{ex} and \mathbf{U}_n denote the numerical solution and the corresponding exact one, respectively.

Summing the resulted errors for each monomial, we can then obtain the error \mathbf{e} as

$$\begin{aligned} \mathbf{e} &= \sum_{n=1}^M a_n \mathbf{e}_n = \mathbf{E} \mathbf{a}, \\ \mathbf{E} &= [\mathbf{e}_1 \quad \mathbf{e}_2 \quad \dots \quad \mathbf{e}_M]. \end{aligned} \quad (50)$$

The Euclidian error can be evaluated as

$$\begin{aligned} e^2 &= \frac{1}{N_d} \mathbf{e}^T \mathbf{e} = \frac{1}{N_d} \mathbf{a}^T \mathbf{Q} \mathbf{a}, \\ \mathbf{Q} &= \mathbf{E}^T \mathbf{E}, \end{aligned} \quad (51)$$

where \mathbf{Q} represents a positive semidefinite matrix, and the maximum eigenvalue is derived as

$$[\mathbf{Q} - \lambda_{\text{max}} \mathbf{I}] = 0, \quad (52)$$

where λ_{max} is the maximum eigenvalue and \mathbf{I} is the unit matrix. On condition that the patch test is passed, the error norm and λ_{max} both will be zero.

In this study, we conduct a patch test based on polynomials of first order, hence taking $m = 1$ in equation (47) leads to

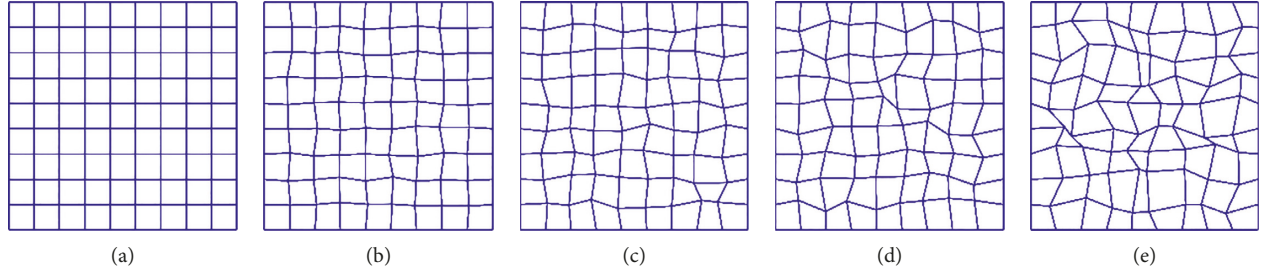


FIGURE 3: Regular and irregular meshes for patch test: (a) regular; (b) irregularity coefficient $\alpha_r = 0.1$; (c) irregularity coefficient $\alpha_r = 0.2$; (d) irregularity coefficient $\alpha_r = 0.3$; (e) irregularity coefficient $\alpha_r = 0.4$.

TABLE 2: Displacement error norm of numerical results for standard patch test on different meshes.

Solution	Regular	Irregular $\alpha_r = 0.1$	Irregular, $\alpha_r = 0.2$	Irregular, $\alpha_r = 0.3$	Irregular, $\alpha_r = 0.4$
λ_{\max}	5.45×10^{-5}	8.72×10^{-5}	1.72×10^{-4}	2.59×10^{-4}	3.45×10^{-4}

$$u^{\text{ex}} = a_0 + a_1 x + a_2 y. \quad (53)$$

We choose a $[-1,1] \times [-1,1]$ square patch domain using 10×10 regular nodes and 100 irregular nodes as shown in Figure 3. For irregular interior nodes, the corresponding coordinates can be obtained as

$$\begin{aligned} x' &= x + \Delta x \cdot r_c \cdot \alpha_r, \\ y' &= y + \Delta y \cdot r_c \cdot \alpha_r, \end{aligned} \quad (54)$$

where Δx and Δy are the initial regular meshes' sizes along x and y axes, respectively. r_c denotes a random number between -1.0 and 1.0 and α_r is a prescribed irregularity factor between 0.0 and 0.5 . A larger α_r value means a more irregular shape of generated meshes in the patch. Table 2 shows that the present method can produce the liner displacement field.

4.2. Example 2: Cantilever Beam Subjected to Tip-Shear Force. A cantilever beam with length L and height D is investigated as a benchmark problem. In this test, the system is subjected to a parabolic traction at the free end as shown in Figure 4. The beam is assumed to have a unit thickness satisfying the plane stress condition. The analytical displacement solution is described in detail by Timoshenko and Goodier [63]:

$$u_x = \frac{Py}{6EI} \left[(6L - 3x)x + (2 + \nu) \left(y^2 - \frac{D^2}{4} \right) \right], \quad (55)$$

$$u_y = -\frac{P}{6EI} \left[3\nu y^2 (L - x) + \frac{1}{4} (4 + 5\nu) D^2 x + x^2 (3L - x) \right], \quad (56)$$

where the moment of inertia I of the beam is given by $I = D^3/12$.

The corresponding stresses are

$$\sigma_x = \frac{P(L-x)y}{I}, \quad (57)$$

$$\sigma_y = 0, \quad (58)$$

$$\tau_{xy} = -\frac{P}{2I} \left(\frac{D^2}{4} - y^2 \right). \quad (59)$$

The parameters are $E = 3.0 \times 10^7$ kPa, $\nu = 0.3$, $D = 12$ m, $L = 48$ m, and $P = -1000$ N.

During the computational process, the nodes on the left boundary are constrained using the exact displacements obtained from equations (55) and (56). The distributed parabolic shear stresses, expressed as equations (57)–(59), acted on the right boundary.

To compare with other methods for convenience in the following examples, we use FE-Meshfree (QS) to denote the presented method, i.e., FE-Meshfree with QS kernel function. Figure 5 shows the steady condition number for different θ , especially $\theta > 10$. As shown in Figure 6, if the irregularity factor $\alpha_r < 0.2$, the errors of the deflection of point A are almost same. If the irregularity factor $\alpha_r > 0.2$, the error increases as the factor increases. The convergence of the strain energy is shown in Figure 7. The convergence rates of displacement and energy error norms are shown in Figures 8 and 9. As expected, the FEM-QUAD4 modes are overly stiff and hence produced lower bounds. The FE-Meshfree (QS) shows a very close-to-exact stiffness and hence very accurate results. The strain energy, displacement, and energy error norms of the FE-Meshfree (QS) are all better than those of the FEM-QUAD4.

Figure 10 shows the computation time of different methods using the same direct solver with the same sets of nodes. FE-Meshfree (QS) takes longer to compute than FEM-QUAD4. However, Figures 11 and 12 show that the efficiency of computation (i.e., computation time necessary for the same accuracy) in terms of both energy and displacement error norms is superior in FE-Meshfree (QS) compared to FEM-QUAD4.

4.3. Example 3: Cantilever Beam Free Vibration Analysis. As shown in Figure 13, a cantilever beam fixed on the left end with length $L = 100$ m and height $H = 10$ m is conducted here as a benchmark problem. The plane stress condition is

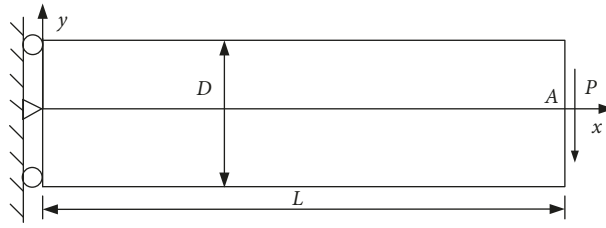


FIGURE 4: Cantilever beam problem.

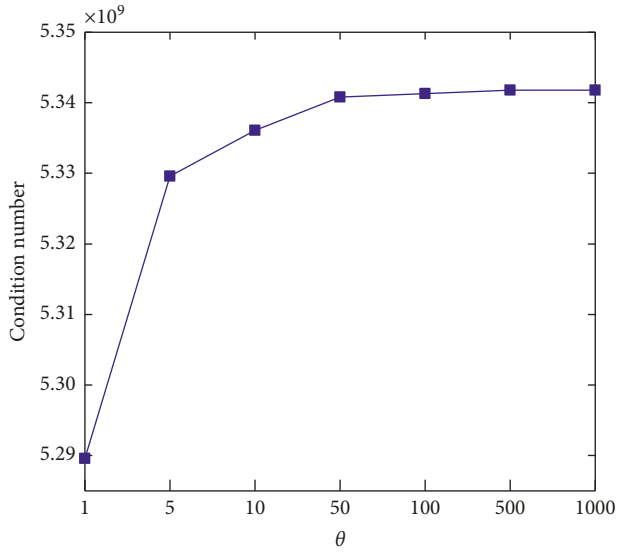


FIGURE 5: Condition number.

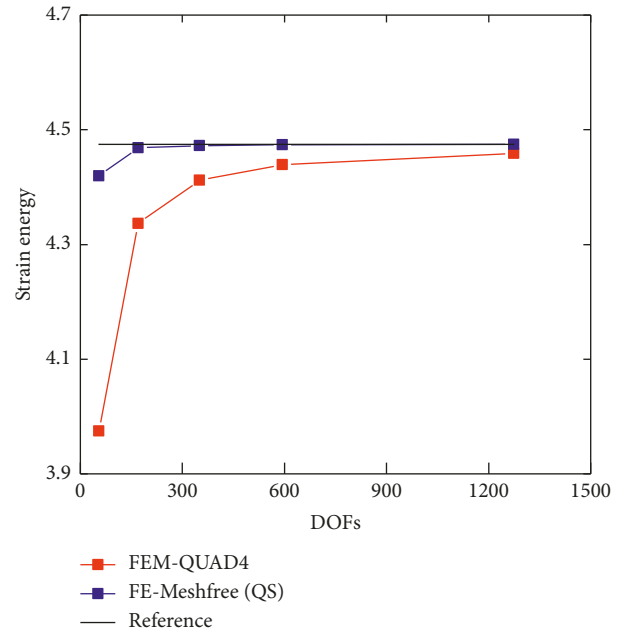


FIGURE 7: Strain energy convergence.

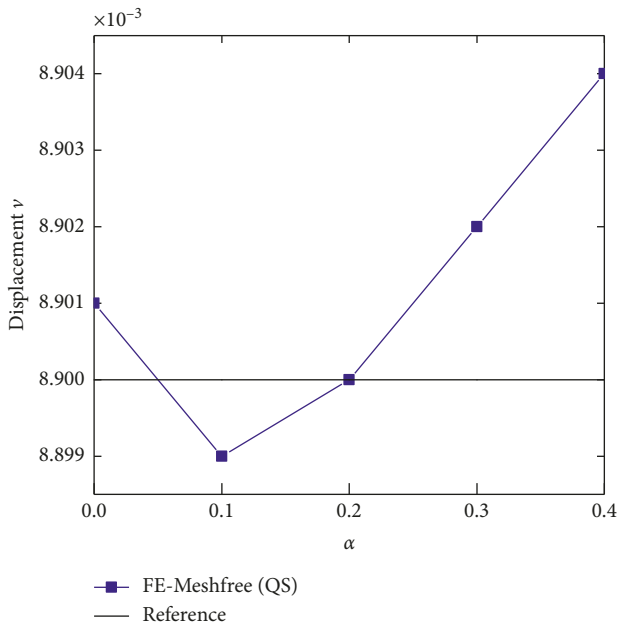


FIGURE 6: Deflection of point A for irregular mesh.

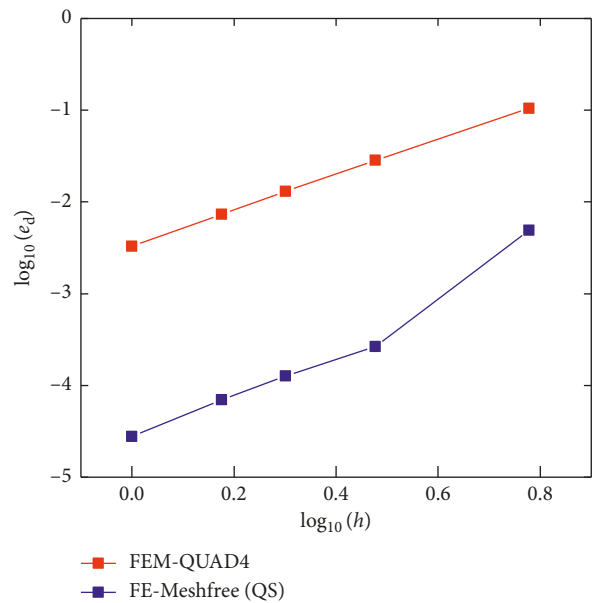


FIGURE 8: Convergence rate of displacement error norms.

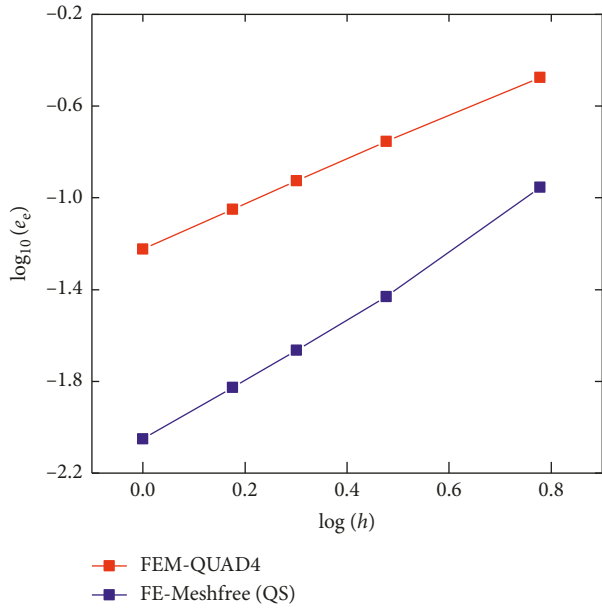


FIGURE 9: Energy error norm convergence.

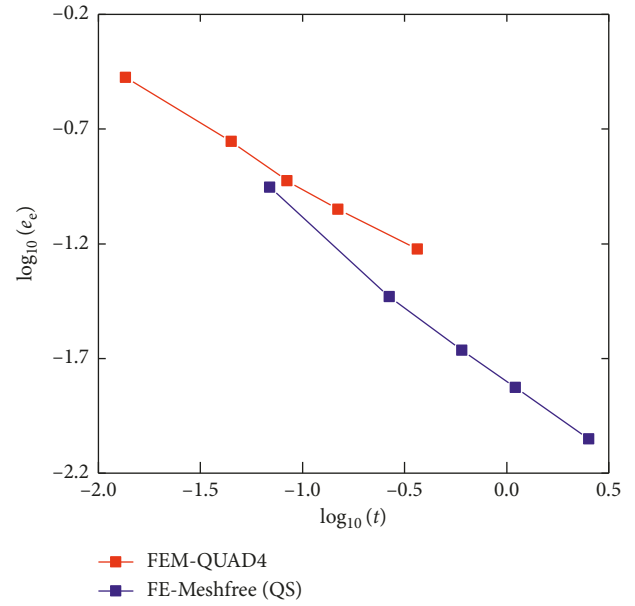


FIGURE 11: Energy error norm with respect to computation time.

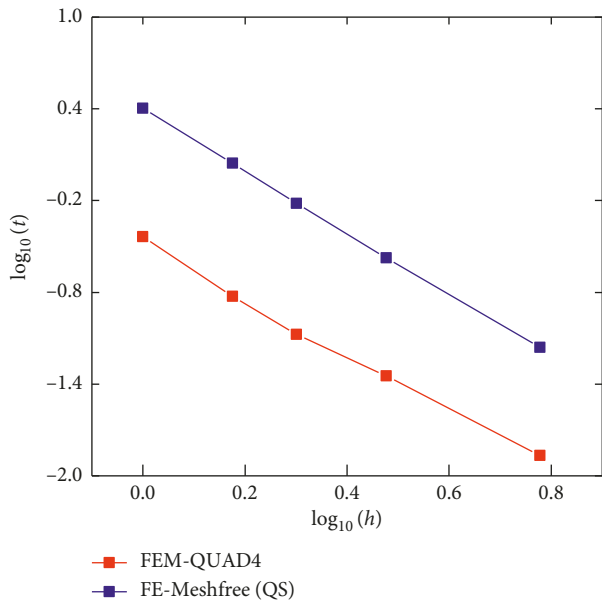


FIGURE 10: Computation time.

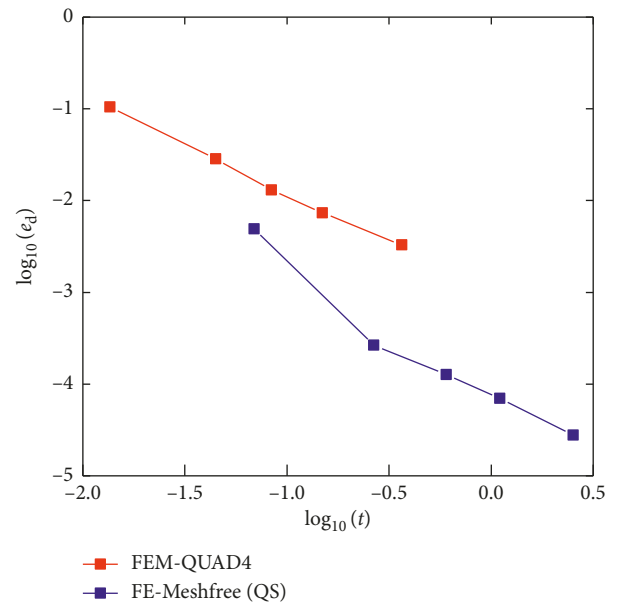


FIGURE 12: Displacement error norm with respect to computation time.

considered. The relative geometrical and material parameters can be summarized as follows: thickness $t = 1.0$ m, Young's modulus $E = 2.1 \times 10^4$ N/m², Poisson's ratio $\nu = 0.3$, and mass density $\rho = 8.0 \times 10^{-10}$ kg/m³. Based on the Euler-Bernoulli beam theory, the fundamental frequency $f_1 = 0.08276 \times 10^4$ Hz can be obtained as a reference.

4.3.1. Effect of the Correlation Parameter θ . The effects of the correlation parameter θ in the modified RPIM on the solution accuracy and stability property are investigated here. The parameter sensitivity analysis of the free vibration of a cantilever beam is conducted by employing 50×5 meshes (Figure 14), in which the correlation parameter θ is set to

be ranged from 1 to 1,000. The first 12 frequencies of the problems determined using various θ , for comparison against the reference fundamental frequency solutions are tabulated in Table 3. Results show great agreement with the exact solutions and high stability regardless of the correlation parameter. Furthermore, nearly the same results are obtained for $\theta \geq 10$. This unique feature of the presented radial basis function enables constant results for any correlation parameter. Accordingly, correlation parameter $\theta = 10$ is used for all subsequent computations.

4.3.2. Convergence Study. For the convergence rates, several types of regular meshes using FEM-QUAD4, FE-Meshfree

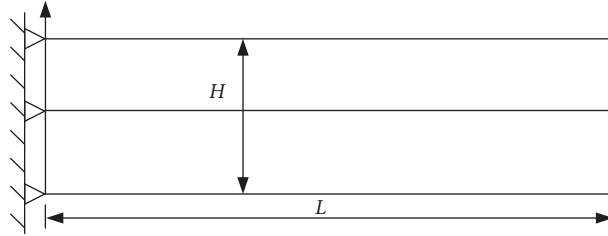


FIGURE 13: Cantilever beam problem.

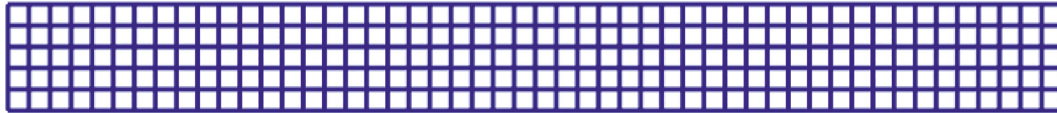


FIGURE 14: Domain discretization of beam using four-node element with regular elements.

TABLE 3: First 12 natural frequencies ($\times 10^4$ Hz) for different correlation parameters θ .

	$\theta = 1$	$\theta = 5$	$\theta = 10$	$\theta = 50$	$\theta = 100$	$\theta = 500$	$\theta = 1000$
f_1	0.0821	0.0822	0.0823	0.0823	0.0823	0.0823	0.0823
f_2	0.4937	0.4936	0.4937	0.4938	0.4938	0.4938	0.4938
f_3	1.2826	1.2826	1.2826	1.2826	1.2826	1.2826	1.2826
f_4	1.3038	1.3008	1.3010	1.3011	1.3012	1.3012	1.3012
f_5	2.3770	2.3653	2.3655	2.3656	2.3657	2.3657	2.3657
f_6	3.6374	3.6093	3.6094	3.6094	3.6094	3.6095	3.6095
f_7	3.8458	3.8450	3.8450	3.8450	3.8450	3.8450	3.8450
f_8	5.0252	4.9719	4.9716	4.9715	4.9715	4.9714	4.9714
f_9	6.4024	6.3985	6.3984	6.3983	6.3983	6.3983	6.3983
f_{10}	6.5005	6.4124	6.4116	6.4112	6.4111	6.4111	6.4111
f_{11}	8.0361	7.9033	7.9019	7.9009	7.9008	7.9008	7.9008
f_{12}	8.9455	8.9350	8.9347	8.9345	8.9345	8.9345	8.9345

(MQ), FE-Meshfree (Exp), are illustrated against the proposed method in this part. Four discrete mesh conditions with regular grids are considered as follows: 10×1 , 20×2 , 50×5 , and 100×10 . The first 12 natural frequencies computed for the four meshes are tabulated in Tables 4–7. The reference results shown in the last column of Table 4 are gathered in the ABAQUS QUAD8 with 200×20 elements. Results show that the proposed method outperforms the other methods. In addition, the performance of FE-Meshfree (MQ) and FE-Meshfree (Exp) is also sensitive to the corresponding relation parameters.

Figure 15 shows an error plot of the first two natural frequencies obtained using the proposed method as well as FEM-QUAD4, FE-Meshfree (MQ), and FE-Meshfree (Exp). Results show that the corresponding error of the proposed method is generally lower than that of other methods. Even for the coarse mesh, the results of the proposed method still show better consistence with the reference solution. Figure 16 displays the first 12 eigenmodes obtained for FE-Meshfree (QS) using the 20×2 meshes. These modeshape plots are in accordance with previously published results for ES-FEM [21].

4.3.3. Sensitivity to Distorted Meshes. The cantilever beam with irregular mesh shown in Figure 13 is also employed to verify the effectiveness of the proposed method. As shown in Figure 17, four distorted meshes with 50×5 elements are used

to assess the influence of mesh quality. Table 8 gives the comparison results of the computed natural frequencies for the first 12 natural frequencies. A comparison of relative error in the computed natural frequencies is shown in Figure 18. As α_r increases, the accuracy of FEM-QUAD4 decreases, whereas the FE-Meshfree (QS) does not show markedly deviation from their original (high) accuracy, indicating great robustness of the proposed method to mesh distortion phenomena.

4.4. Example 4: Shear Wall Free Vibration Analysis. In this part, a shear wall with four openings, as shown in Figure 19 is investigated. The parameters in the computation include Young's modulus $E = 10000$ N/m², Poisson's ratio $\nu = 0.2$, thickness $t = 1.0$ m, and mass density $\rho = 1.0$ kg/m³. The bottom edge is fully clamped, and a plane stress case is considered here. The mesh for computation with 476 elements and 559 nodes is shown in Figure 20. This problem was analyzed previously using a boundary element method by Brabbia et al. [64] and also by Liu and Gu [13] using a local radial point interpolation method with the multiquadrics radial function. The commercial software applications, ANSYS and ABAQUS, are employed here for comparison.

The natural frequencies of the first eight modes are tabulated in Table 9. The results show great agreement with those obtained by other methods. Figure 21 displays the first eight

TABLE 4: Natural frequencies ($\times 10^4$ Hz) of a cantilever beam for 10 elements.

Number of elements	Number of nodes	FEM-QUAD4	FE-Meshfree (QS, $\theta = 10$)	FE-Meshfree (MQ, $b = 1 \times 10^{-4}, q = 2.01$)	FE-Meshfree (MQ, $b = 1.0, q = 2.01$)	FE-Meshfree (Exp, $b = 1.0$)	FE-Meshfree (Exp, $b = 0.1$)	Reference (ABAQUS Quad8)	
(10 × 1)	10	22	0.1000	0.0824	0.0825	0.0909	0.1130	0.0848	0.0822
			0.6077	0.5058	0.5050	0.5455	0.6732	0.5120	0.4931
			1.2863	1.2846	1.2844	1.2849	1.2858	1.2839	1.2823
			1.6422	1.3672	1.3621	1.4281	1.7140	1.3539	1.2990
			3.0958	2.5583	2.5437	2.5729	2.9437	2.4719	2.3607
			3.8918	3.8421	3.8430	3.8384	3.8596	3.8071	3.6002
			4.9311	4.0208	3.9947	3.9079	4.2015	3.8405	3.8442
			6.5947	5.6927	5.6693	5.4218	5.4614	5.3572	4.9566
			7.1110	6.3692	6.3762	6.3422	6.4073	6.3656	6.3897
			9.4517	7.5079	7.5313	7.1592	6.8653	7.1909	6.3972
			9.5747	8.8600	8.8821	8.7702	8.6496	8.8518	7.8719
12.188	9.4823	9.6067	9.1641	9.8540	9.4100	8.9331			

TABLE 5: Natural frequencies ($\times 10^4$ Hz) of a cantilever beam for 40 elements.

Number of elements	Number of nodes	FEM-QUAD4	FE-Meshfree (QS, $\theta = 10$)	FE-Meshfree (MQ, $b = 1 \times 10^{-4}, q = 2.01$)	FE-Meshfree (MQ, $b = 1.0, q = 2.01$)	FE-Meshfree (Exp, $b = 1.0$)	FE-Meshfree (Exp, $b = 0.1$)	Reference (ABAQUS Quad8)	
(20 × 2)	40	63	0.0872	0.0824	0.0825	0.0875	0.0981	0.0849	0.0822
			0.5263	0.4981	0.4986	0.5249	0.5821	0.5112	0.4931
			1.2837	1.2834	1.2834	1.2836	1.2839	1.2831	1.2823
			1.4010	1.3233	1.3255	1.3826	1.5161	1.3523	1.2990
			2.5816	2.4265	2.4325	2.5107	2.7232	2.4680	2.3607
			3.8573	3.7297	3.7423	3.8232	3.8472	3.7767	3.6002
			4.0002	3.8469	3.8472	3.8453	4.1064	3.8463	3.8442
			5.6040	5.1688	5.1903	5.2518	5.5903	5.2123	4.9566
			6.4492	6.3995	6.4018	6.3901	6.3954	6.3995	6.3897
			7.3601	6.7004	6.7325	6.7524	7.1240	6.7308	6.3972
			9.0702	8.2958	8.3397	8.2973	8.6741	8.3043	7.8719
9.2470	8.9314	8.9379	8.9054	8.9147	8.9338	8.9331			

TABLE 6: Natural frequencies ($\times 10^4$ Hz) of a cantilever beam for 250 elements.

Number of elements	Number of nodes	FEM-QUAD4	FE-Meshfree (QS, $\theta = 10$)	FE-Meshfree (MQ, $b = 1 \times 10^{-4}, q = 2.01$)	FE-Meshfree (MQ, $b = 1.0, q = 2.01$)	FE-Meshfree (Exp, $b = 1.0$)	FE-Meshfree (Exp, $b = 0.1$)	Reference (ABAQUS Quad8)	
(50 × 5)	250	306	0.0830	0.0823	0.0822	0.0831	0.0852	0.0827	0.0822
			0.4989	0.4937	0.4936	0.4986	0.5104	0.4962	0.4931
			1.2827	1.2826	1.2826	1.2827	1.2828	1.2825	1.2823
			1.3168	1.3010	1.3005	1.3127	1.3421	1.3063	1.2990
			2.3992	2.3655	2.3640	2.3839	2.4343	2.3726	2.3607
			3.6701	3.6094	3.6064	3.6331	3.7057	3.6165	3.6002
			3.8467	3.8450	3.8449	3.8448	3.8449	3.8445	3.8442
			5.0697	4.9716	4.9667	4.9984	5.0934	4.9765	4.9566
			6.4062	6.3984	6.3983	6.3965	6.3955	6.3971	6.3897
			6.5590	6.4116	6.4043	6.4391	6.5558	6.4121	6.3972
			8.1119	7.9019	7.8918	7.9274	8.0652	7.8957	7.8719
8.9562	8.9347	8.9348	8.9290	8.9251	8.9320	8.9331			

eigenmodes obtained by the proposed method, from which it can be observed that the modeshapes plot match well with those of ES-FEM [21].

4.5. Example 5: Connecting Rod Free Vibration Analysis. Here, we perform free vibration analysis of a connecting rod with a relatively complex configuration in which the

boundary conditions can be clearly observed in Figure 22. The rod is discretized with 723 irregularly distributed nodes, as shown in Figure 23. The plane stress problem is considered with $E = 10$ GPa, $\nu = 0.3$, and $\rho = 7.8 \times 10^3$ kg/m³. A reference solution is also obtained in ABAQUS QUAD8 with 24,149 elements. Table 10 gives the first 10 natural frequencies, where FE-Meshfree (QS) yields comparable results to ABAQUS (similar to the previous example).

TABLE 7: Natural frequencies ($\times 10^4$ Hz) of a cantilever beam for 1000 elements.

Number of elements	Number of nodes	FEM-QUAD4	FE-Meshfree (QS, $\theta = 10$)	FE-Meshfree (MQ, $b = 1 \times 10^{-4}, q = 2.01$)	FE-Meshfree (MQ, $b = 1.0, q = 2.01$)	FE-Meshfree (Exp, $b = 1.0$)	FE-Meshfree (Exp, $b = 0.1$)	Reference (ABAQUS Quad8)
(100 × 10) 1000	1111	0.0824	0.0822	0.0822	0.0824	0.0830	0.0824	0.0822
		0.4947	0.4933	0.4933	0.4943	0.4978	0.4940	0.4931
		1.2825	1.2824	1.2824	1.2824	1.2825	1.2824	1.2823
		1.3037	1.2995	1.2994	1.3019	1.3110	1.3011	1.2990
		2.3707	2.3618	2.3614	2.3654	2.3817	2.3641	2.3607
		3.6183	3.6023	3.6015	3.6068	3.6312	3.6050	3.6002
		3.8450	3.8445	3.8444	3.8445	3.8446	3.8443	3.8442
		4.9858	4.9600	4.9586	4.9649	4.9981	4.9627	4.9566
		6.3996	6.3944	6.3923	6.3972	6.3970	6.3968	6.3897
		6.4332	6.3976	6.3975	6.3992	6.4415	6.3972	6.3972
		7.9335	7.8783	7.8753	7.8822	7.9341	7.8797	7.8719
8.9391	8.9337	8.9337	8.9326	8.9313	8.9328	8.9331		

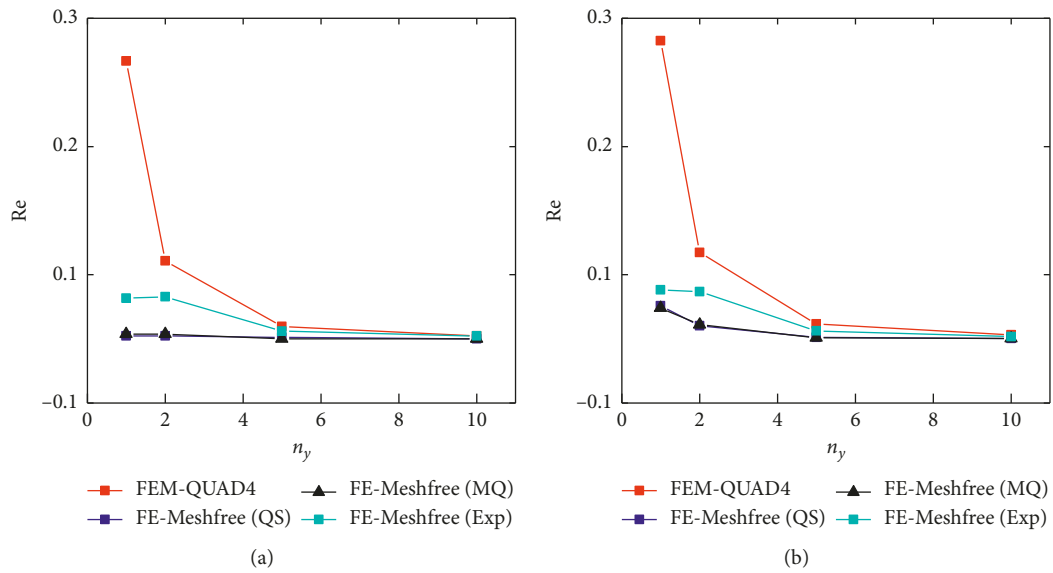


FIGURE 15: Computed first two natural frequencies. (a) Mode 1. (b) Mode 2.

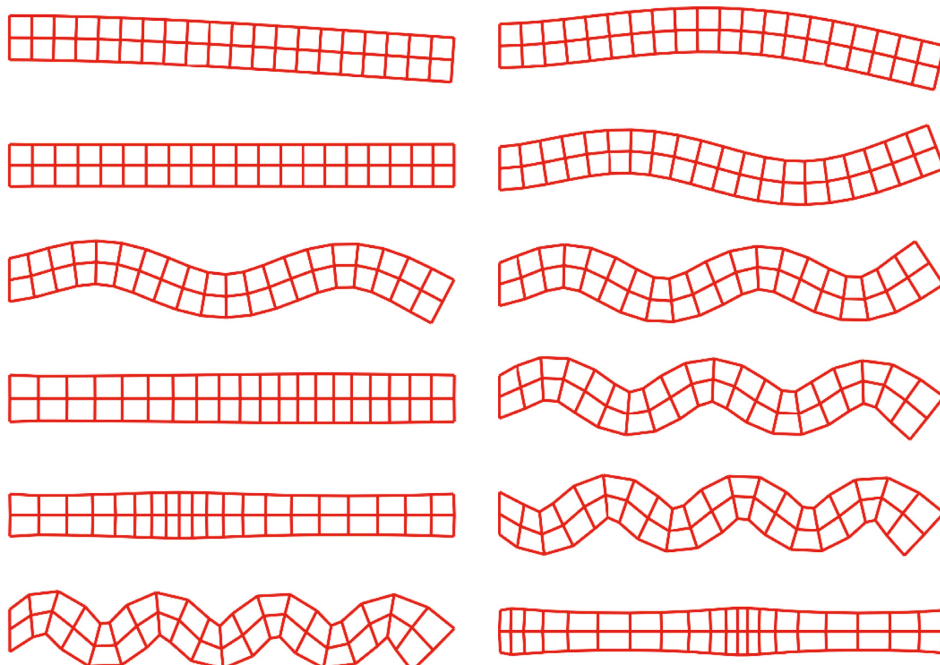


FIGURE 16: First 12 modeshapes of cantilever beam.

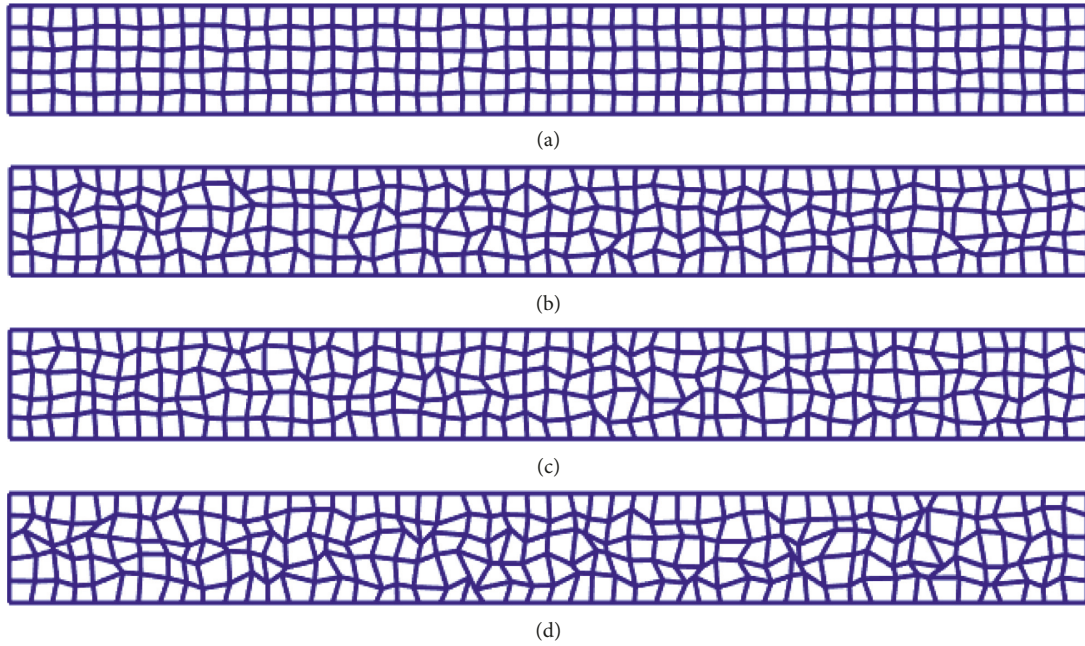


FIGURE 17: Beam domain discretization using four-node element with irregular elements. (a) $\alpha_r = 0.1$. (b) $\alpha_r = 0.2$. (c) $\alpha_r = 0.3$. (d) $\alpha_r = 0.4$.

TABLE 8: First 12 natural frequencies ($\times 10^4$ Hz) of a cantilever beam using irregular nodal distribution (50×5 elements).

Method	$\alpha_r = 0$	$\alpha_r = 0.1$	$\alpha_r = 0.2$	$\alpha_r = 0.3$	$\alpha_r = 0.4$	Reference (ABAQUS QUAD8)
FEM-QUAD4	0.0830	0.0831	0.0834	0.0835	0.0838	0.0822
	0.4989	0.4992	0.5016	0.5019	0.5036	0.4931
	1.2827	1.2827	1.2827	1.2827	1.2827	1.2823
	1.3168	1.3176	1.3243	1.3245	1.3297	1.2990
	2.3992	2.4007	2.4114	2.4139	2.4242	2.3607
	3.6701	3.6725	3.6914	3.6963	3.7096	3.6002
	3.8467	3.8468	3.8470	3.8470	3.8471	3.8442
	5.0697	5.0728	5.0974	5.1059	5.1249	4.9566
	6.4062	6.4063	6.4072	6.4072	6.4074	6.3897
	6.5590	6.5643	6.5999	6.6089	6.6360	6.3972
	8.1119	8.1186	8.1651	8.1733	8.2060	7.8719
	8.9562	8.9565	8.9528	8.9585	8.9606	8.9331
FE-Meshfree (QS, $\theta = 10$)	0.0823	0.0822	0.0822	0.0822	0.0822	0.0822
	0.4937	0.4937	0.4936	0.4936	0.4936	0.4931
	1.2826	1.2826	1.2825	1.2824	1.2822	1.2823
	1.3010	1.3010	1.3008	1.3009	1.3010	1.2990
	2.3655	2.3655	2.3655	2.3655	2.3661	2.3607
	3.6094	3.6092	3.6098	3.6095	3.6113	3.6002
	3.8450	3.8450	3.8445	3.8444	3.8441	3.8442
	4.9716	4.9715	4.9722	4.9728	4.9755	4.9566
	6.3984	6.3984	6.3978	6.3974	6.3966	6.3897
	6.4116	6.4114	6.4126	6.4142	6.4179	6.3972
	7.9019	7.9017	7.9043	7.9039	7.9110	7.8719
	8.9347	8.9346	8.9337	8.9333	8.9331	8.9331

4.6. Example 6: Cantilever Beam Implicit Forced Vibration Analysis. The benchmark cantilever beam and mesh shown in Figures 24 and 25 are investigated via the Bathe method. The plane strain problem is considered with numerical parameters $L = 4.0$ m, $H = 1.0$ m, $t = 1.0$ m, $E = 1.0$ N/m², $\nu = 0.3$, $\rho = 1.0$ kg/m³, $\alpha = 0.005$, and $\beta = 0.272$. The domain is represented by 10×2 elements. The first loading is in the harmonic form with $f(t) = \cos(\omega_f t)$. The corresponding

dynamic responses can be shown in Figures 26 and 27 with $\omega_f = 0.01$ and 0.05 , respectively. Then, a constant step load $f(t) = 1$ is added at the apex from $t = 0$. The time step $\Delta t = 2.0$ is used for time integration. Both damping effect and no damping effect are considered here. A reference solution is obtained in ABAQUS QUAD8 with 2,600 elements.

Per the dynamic responses in Figures 26–28, both methods tested provided nearly identical vibration frequency

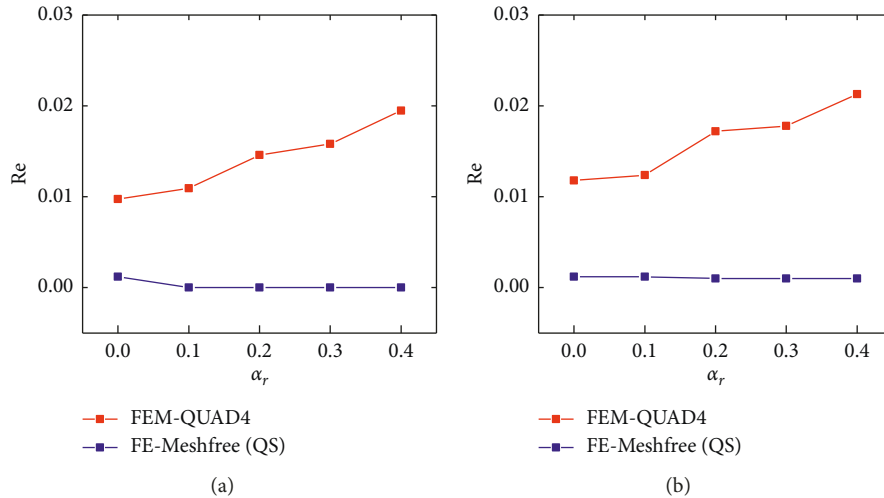


FIGURE 18: Error in the computed first two frequencies for distortion sensitivity test.

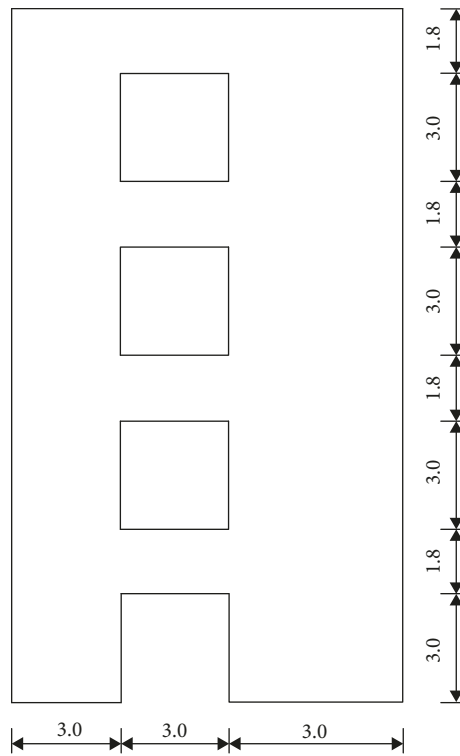


FIGURE 19: Shear wall with four openings.

with the amplitude of FE-Meshfree (QS) being closer to the reference solution. This indicates that the FE-Meshfree (QS) can be readily applied to actual vibration analyses with excellent accuracy, which may be partially due to the fact that the FE-Meshfree (QS) model owns very close-to-exact stiffness.

4.7. Example 7: Spherical Shell Implicit Forced Vibration Analysis. As shown in Figure 29, a spherical shell subjected to a concentrated loading at its apex is examined. In total, 30×3 asymmetric elements are used (Figure 30) with the numerical parameters $R = 12$ m, $t = 0.1$ m,

$\phi = 10.9^\circ$, $E = 1.0$ N/m², $\nu = 0.3$, and $\rho = 1.0$ kg/m³. A reference solution is obtained by ABAQUS QUAD8 with 2,000 elements. The first loading is applied in the harmonic form $f(t) = \cos(\omega_f t)$. Its dynamic responses can be observed from Figures 31 and 32 with $\omega_f = 0.01$ and 0.05, respectively. A constant step load $f(t) = 1$ is then added at the apex from $t = 0$. The time step $\Delta t = 2.0$ is used for time integration. The dynamic responses shown in Figures 31–33 indicate that FE-Meshfree (QS) is more accurate than FEM-QUAD4. It yields results very close to the reference one for both damping and no damping effect situations.

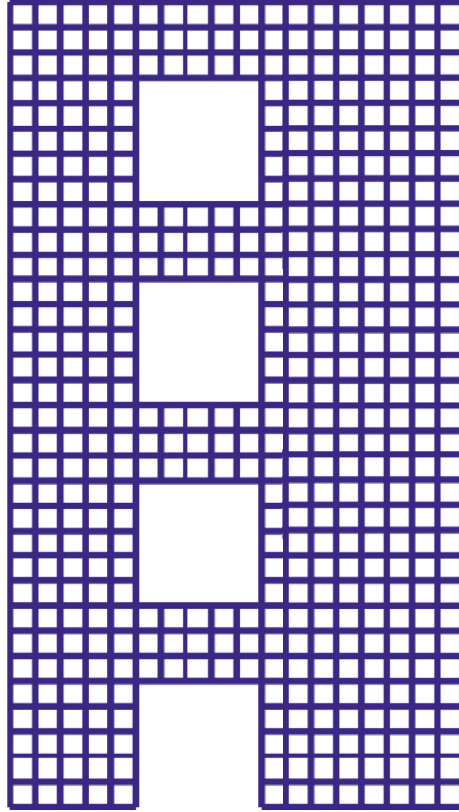


FIGURE 20: Model of shear wall with four openings.

TABLE 9: Natural frequencies (rad/s) of shear wall.

Model	FEM-QUAD4	FE-Meshfree (QS)	LRPIM (MQ) [13]	Brebbia (BEM) [64]	ANSYS [49]	ABAQUS	QUAD4-CNS [50]
1	2.074	2.085	2.086	2.079	2.057	2.073	2.094
2	7.114	7.117	7.152	7.181	7.067	7.096	7.124
3	7.627	7.632	7.647	7.644	7.620	7.625	7.590
4	11.978	12.063	12.019	11.833	11.840	11.938	12.192
5	15.444	15.410	15.628	15.947	15.313	15.341	15.451
6	18.429	18.351	18.548	18.644	18.342	18.345	18.330
7	19.991	19.882	20.085	20.268	19.887	19.876	19.858
8	22.348	22.258	22.564	22.765	22.236	22.210	22.225

5. Conclusions

In this study, FE-Meshfree QUAD4 element with modified radial point interpolation function has been extended to the free vibration and forced vibration analysis of 2D solids. Based on the above simulations, we can make the following conclusions:

- (1) Compared to meshfree methods, the composite shape function of FE-Meshfree QUAD4 element with modified radial point interpolation function possess the much desired Kronecker delta property. Therefore, the essential boundary conditions can be easily applied as in the FEM.
- (2) As in the classical FEM, the shape function of FE-Meshfree possesses the much desired Kronecker delta property, and accordingly the essential

boundary conditions can be easily applied. Moreover, higher-order global approximations can be readily achieved without the addition of extra nodes or DOFs.

- (3) The normalized radial basis function yields composite shape functions without any tuning parameters and thus can be used to approximate displacement fields.
- (4) Compared to the FEM-QUAD4, the mesh distortion test (Section 4.3.3) shows that the error of the proposed method is insensitive to the increase of the distortion parameters, indicating better robustness to mesh distortion of the proposed method.
- (5) The proposed method enables to obtain more accurate free vibration analysis results at a higher convergence rate. In addition, the vibration period

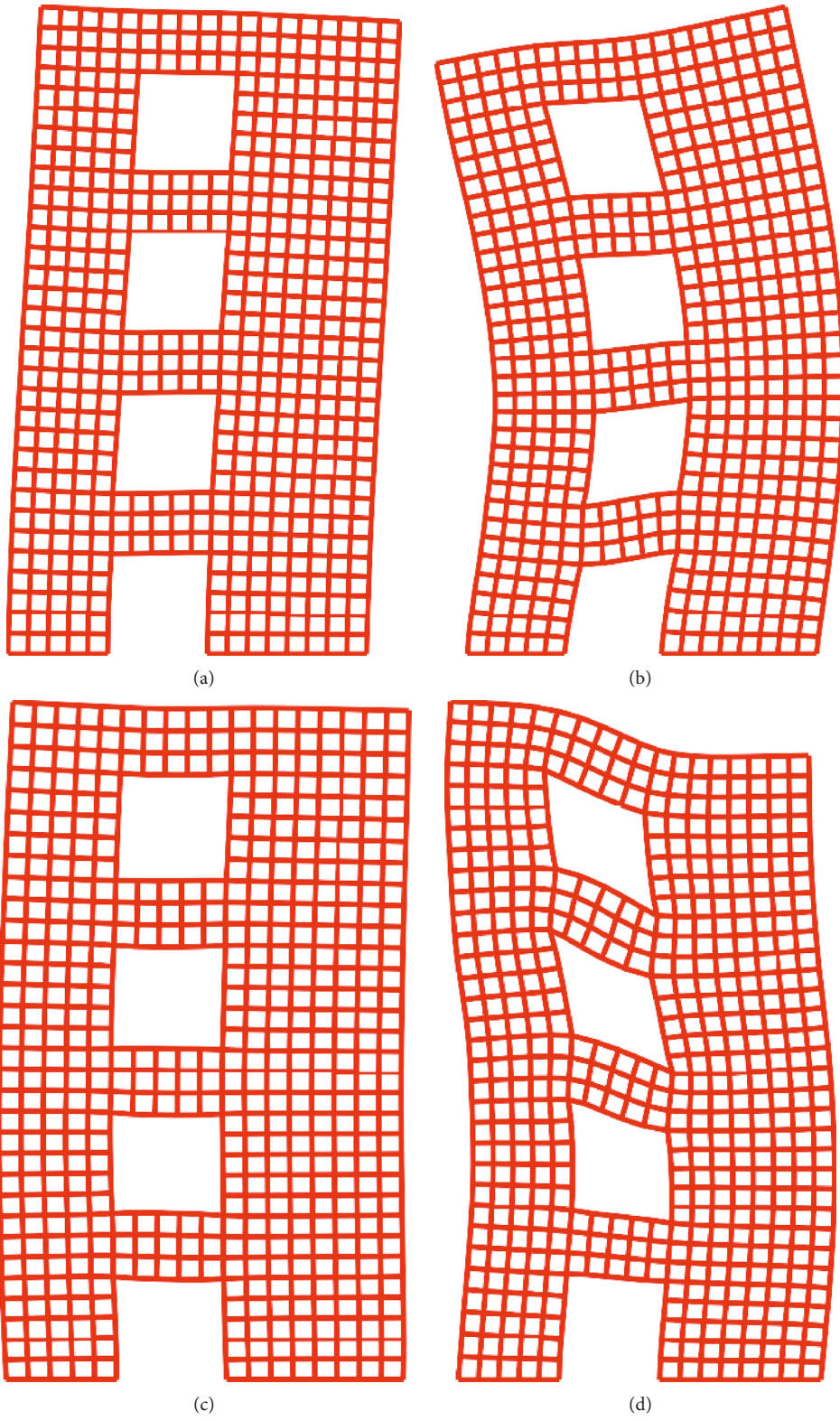


FIGURE 21: Continued.

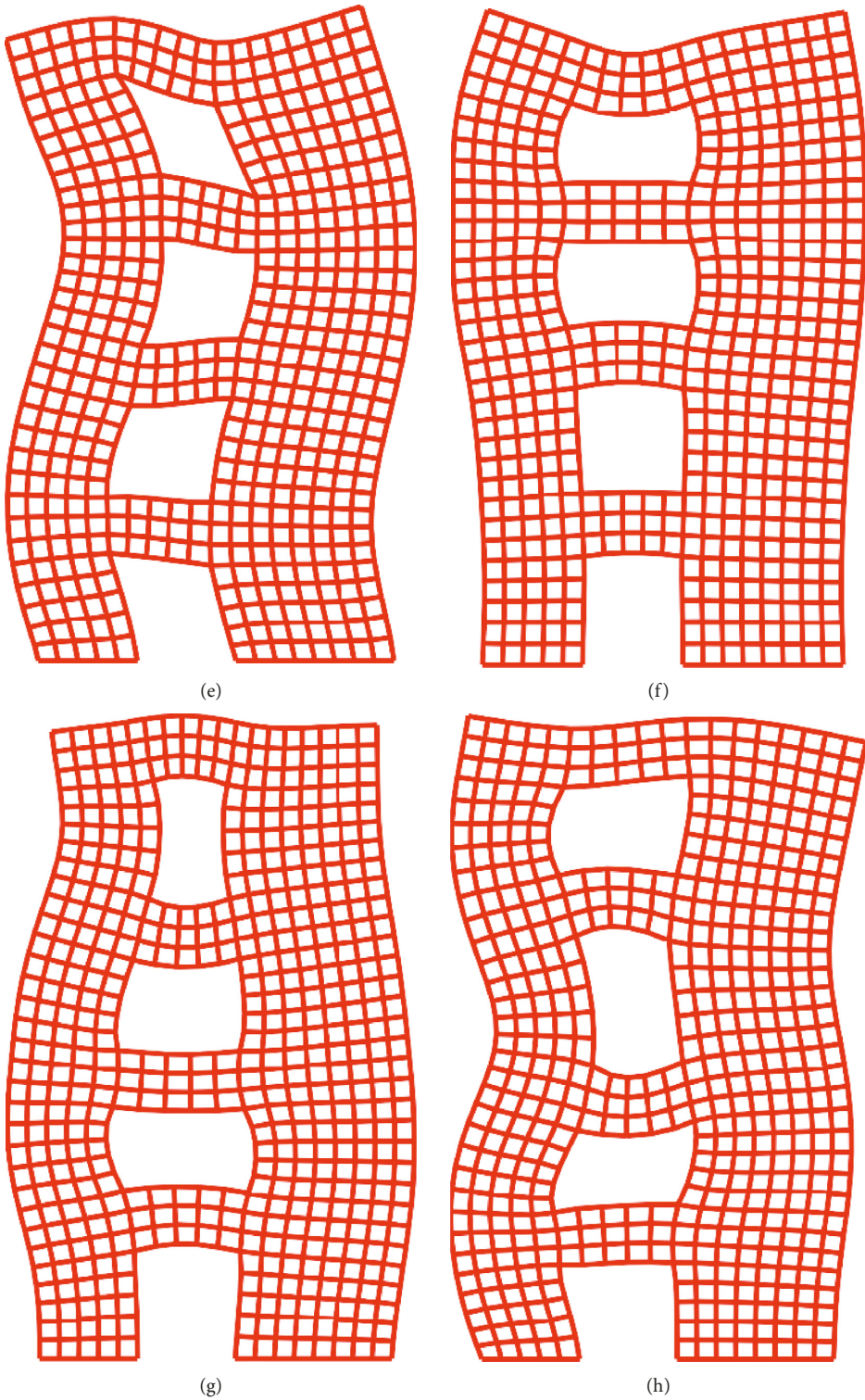


FIGURE 21: First 8 modeshapes of shear wall with four openings. (a) Mode 1. (b) Mode 2. (c) Mode 3. (d) Mode 4. (e) Mode 5. (f) Mode 6. (g) Mode 7. (h) Mode 8.

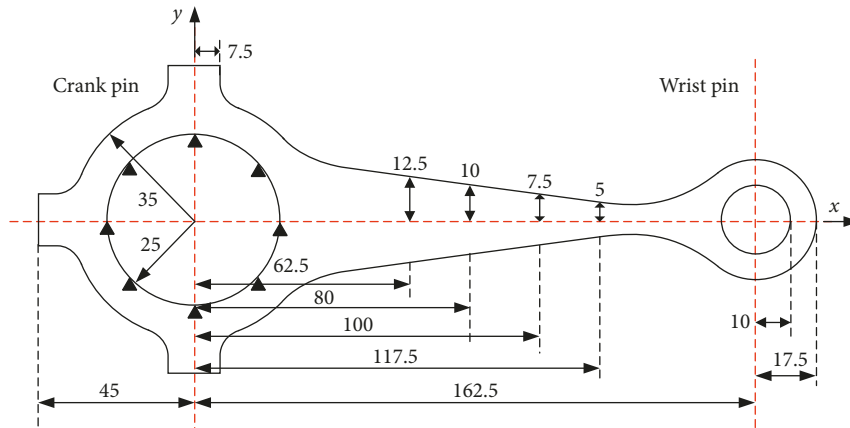


FIGURE 22: Geometric model and boundary conditions of automotive connecting rod.

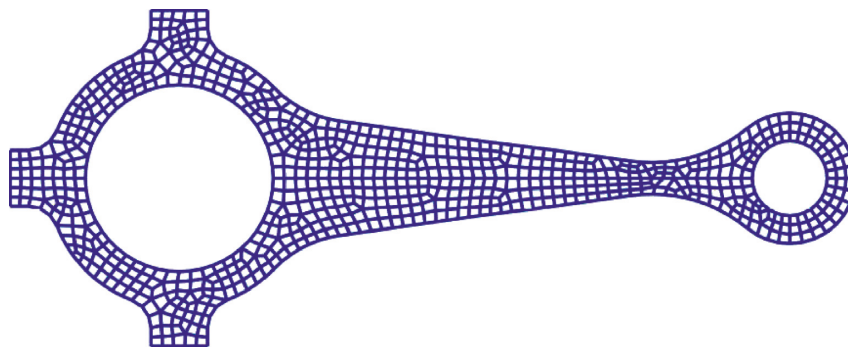


FIGURE 23: Domain discretization of connecting bar using four-node elements.

TABLE 10: First ten natural frequencies ($\times 10^6$ rad/s) of connecting rod.

Mode	FEM-QUAD4	FE-Meshfree (QS)	Reference (ABAQUS QUAD8)
1	1.3673	1.3592	1.3418
2	2.8093	2.7995	2.7042
3	3.9773	3.9289	3.7932
4	4.1908	4.1890	4.1078
5	5.7172	5.6162	5.5291
6	7.3185	7.3137	7.0938
7	7.8352	7.6765	7.5696
8	8.2621	8.2325	8.1509
9	8.4762	8.4387	8.3444
10	8.6747	8.6310	8.5351

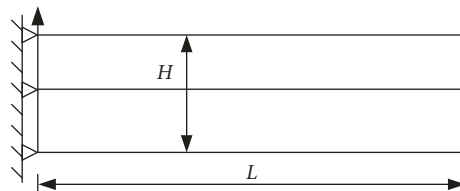


FIGURE 24: Cantilever beam.

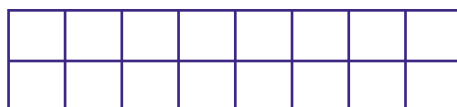


FIGURE 25: Domain discretization of cantilever beam.

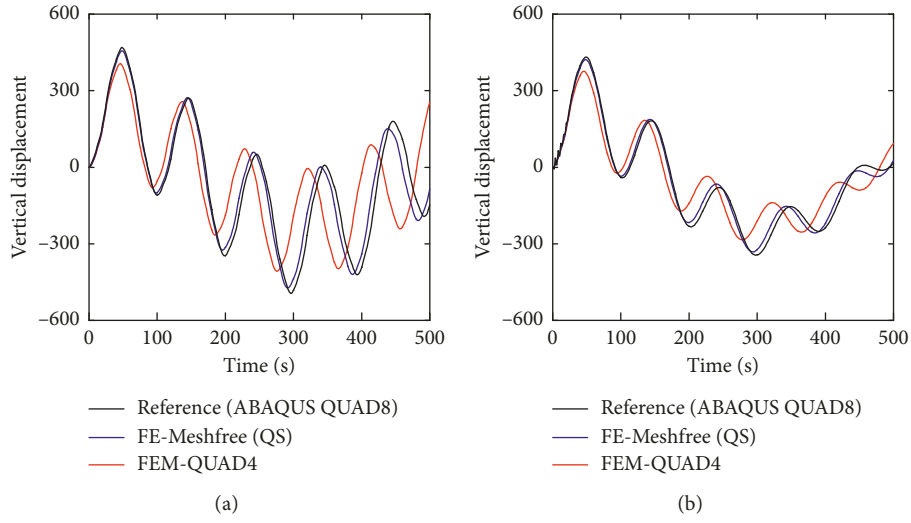


FIGURE 26: Transient response of cantilever beam subjected to harmonic loading with $\omega_f = 0.01$: (a) without damping; (b) with damping.

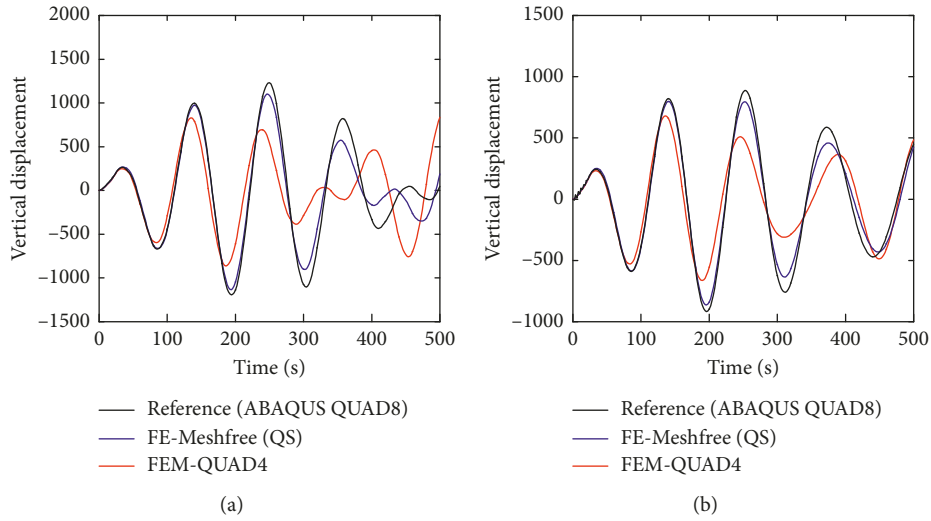


FIGURE 27: Transient response of cantilever beam subjected to harmonic loading with $\omega_f = 0.05$: (a) without damping; (b) with damping.

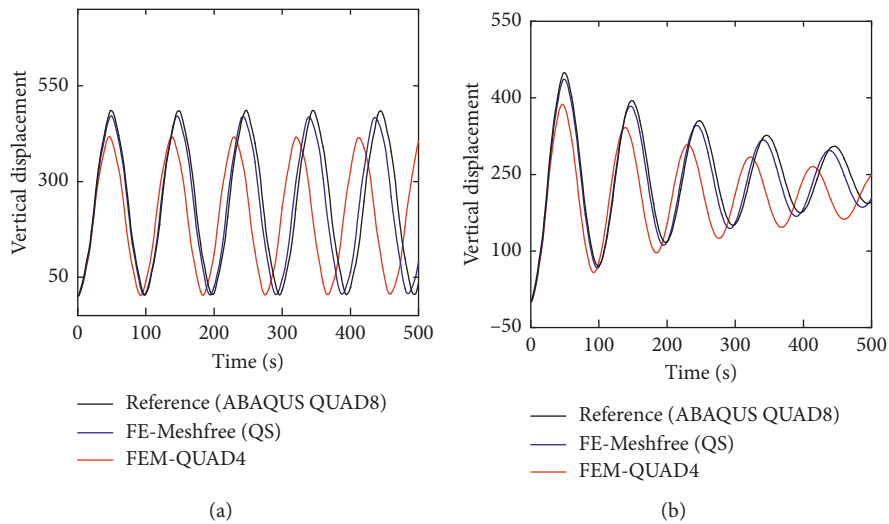


FIGURE 28: Transient response of cantilever beam subjected to constant step loading: (a) without damping; (b) with damping.

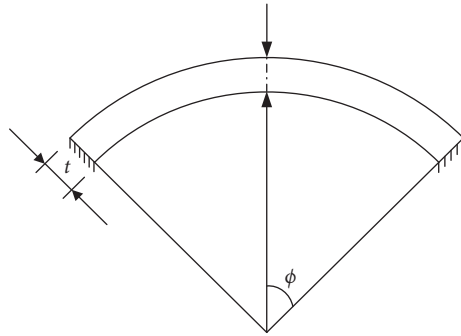


FIGURE 29: Spherical shell.



FIGURE 30: Domain discretization of half of the spherical shell.

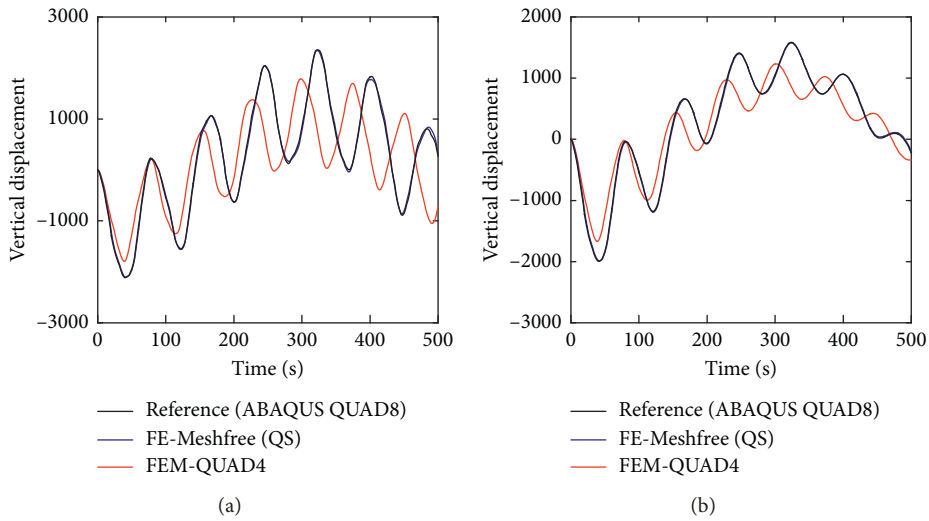


FIGURE 31: Transient response of spherical shell subjected to harmonic loading with $\omega_f = 0.01$: (a) without damping; (b) with damping.

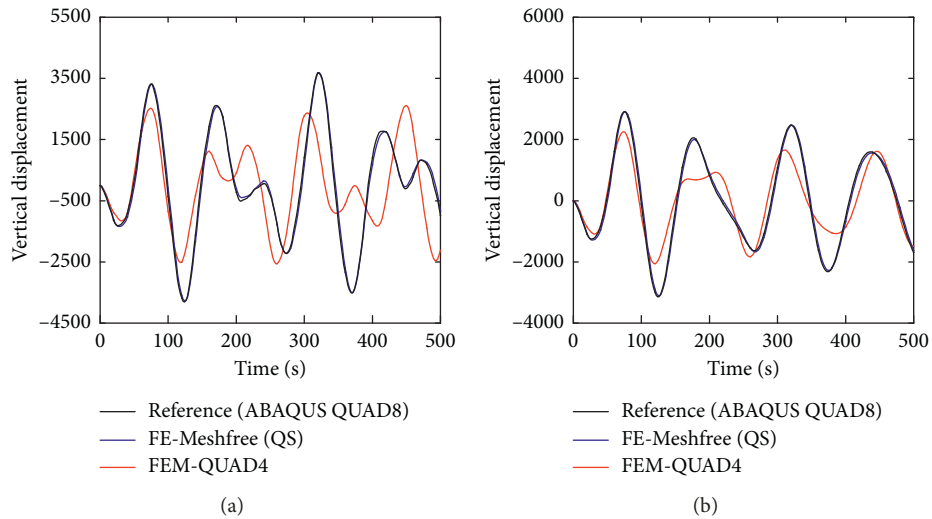


FIGURE 32: Transient response of spherical shell subjected to harmonic loading with $\omega_f = 0.05$: (a) without damping; (b) with damping.

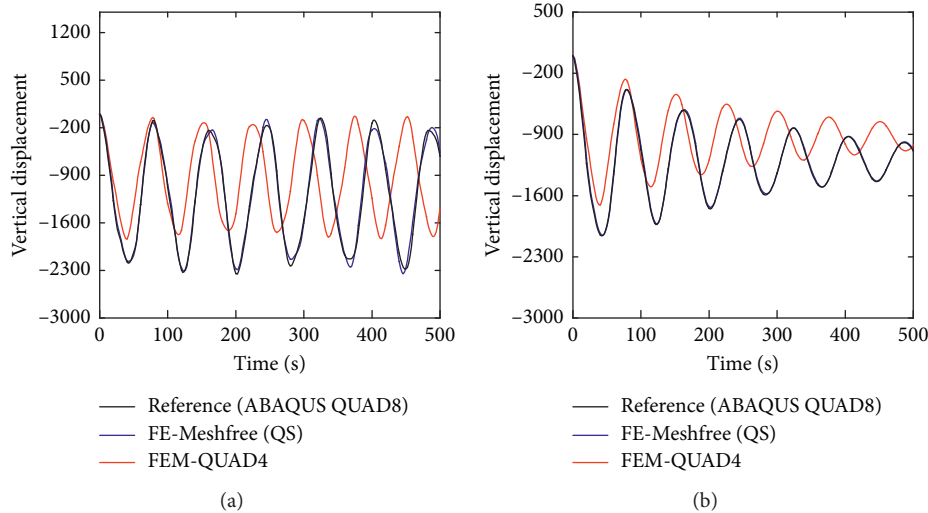


FIGURE 33: Transient response of spherical shell subjected to constant step loading: (a) without damping; (b) with damping.

obtained for forced vibration analysis is very close to the reference ones.

Although the presented method works well in 2D linear elastic, free vibration, and forced vibration problems, most problems are 3D (solid, plate, shell, etc.) in reality. Formulations and numerical tests of these elements will be presented and applied for more complex problems in our following work.

Data Availability

The data used to support the findings of this study are available from the corresponding author upon request.

Conflicts of Interest

The authors declare that they have no conflicts of interest.

Acknowledgments

This study was supported by the National Natural Science Foundation of China under grant no. 11472137 and the Fundamental Research Funds for the Central Universities under grant no. 309181A8801.

References

- [1] T. R. Hughes, *The Finite Element Method—Linear Static and Dynamic Finite Element Analysis*, Prentice-Hall, Englewood Cliff, NJ, USA, 1987.
- [2] K. J. Bathe, *Finite Element Procedures*, Prentice-Hall, Englewood Cliffs, New Jersey, 1996.
- [3] O. C. Zienkiewicz and R. L. Taylor, *The Finite Element Method*, Butterworth-Heinemann, Oxford, UK, 5th edition, 2000.
- [4] N.-S. Lee and K.-J. Bathe, “Effects of element distortions on the performance of isoparametric elements,” *International Journal for Numerical Methods in Engineering*, vol. 36, no. 20, pp. 3553–3576, 1993.
- [5] W. Zeng and G. R. Liu, “Smoothed finite element methods (S-FEM): an overview and recent developments,” *Archives of Computational Methods in Engineering*, vol. 25, no. 2, pp. 1–39, 2016.
- [6] V. P. Nguyen, T. Rabczuk, S. Bordas, and M. Duflot, “Meshless methods: a review and computer implementation aspects,” *Mathematics and Computers in Simulation*, vol. 79, no. 3, pp. 763–813, 2008.
- [7] R. A. Gingold and J. J. Monaghan, “Smoothed particle hydrodynamics: theory and application to non-spherical stars,” *Monthly Notices of the Royal Astronomical Society*, vol. 181, no. 3, pp. 375–389, 1977.
- [8] T. Belytschko, Y. Y. Lu, and L. Gu, “Element-free Galerkin methods,” *International Journal for Numerical Methods in Engineering*, vol. 37, no. 2, pp. 229–256, 1994.
- [9] W. K. Liu, S. Jun, and Y. F. Zhang, “Reproducing kernel particle methods,” *International Journal for Numerical Methods in Fluids*, vol. 20, no. 8-9, pp. 1081–1106, 1995.
- [10] S. N. Atluri and T. Zhu, “A new meshless local Petrov-Galerkin (MLPG) approach in computational mechanics,” *Computational Mechanics*, vol. 22, no. 2, pp. 117–127, 1998.
- [11] D. Mirzaei and K. Hasanpour, “Direct meshless local Petrov-Galerkin method for elastodynamic analysis,” *Acta Mechanica*, vol. 227, no. 3, pp. 1–14, 2016.
- [12] G. R. Liu and Y. T. Gu, “A point interpolation method for two-dimensional solids,” *International Journal for Numerical Methods in Engineering*, vol. 50, no. 4, pp. 937–951, 2001.
- [13] G. R. Liu and Y. T. Gu, “A local radial point interpolation method (Lrpim) for free vibration analyses of 2-D solids,” *Journal of Sound and Vibration*, vol. 246, no. 1, pp. 29–46, 2001.
- [14] J. O. Daniel, K. Danielson, and N. Boone, “Modeling fragment simulating projectile penetration into steel plates using finite elements and meshfree particles,” *Shock and Vibration*, vol. 18, no. 3, pp. 425–436, 2013.
- [15] A. Shojaei, T. Mudric, M. Zaccariotto, and U. Galvanetto, “A coupled meshless finite point/Peridynamic method for 2D dynamic fracture analysis,” *International Journal of Mechanical Sciences*, vol. 119, pp. 419–431, 2016.

- [16] G. R. Liu, K. Y. Dai, and T. T. Nguyen, "A smoothed finite element method for mechanics problems," *Computational Mechanics*, vol. 39, no. 6, pp. 859–877, 2006.
- [17] J.-S. Chen, C.-T. Wu, S. Yoon, and Y. You, "A stabilized conforming nodal integration for Galerkin mesh-free methods," *International Journal for Numerical Methods in Engineering*, vol. 50, no. 2, pp. 435–466, 2000.
- [18] K. You, J. H. Lim, D. Sohn, and S. Im, "A three-dimensional cell-based smoothed finite element method for elasto-plasticity," *Journal of Mechanical Science and Technology*, vol. 29, no. 2, pp. 611–623, 2015.
- [19] G. R. Im, T. Nguyen-Thoi, H. Nguyen-Xuan, and K. Y. Lam, "A node-based smoothed finite element method (NS-FEM) for upper bound solutions to solid mechanics problems," *Computers and Structures*, vol. 87, no. 1-2, pp. 14–26, 2009.
- [20] T. T. Lam, H. C. Vu-Do, T. Rabczuk et al., "A node-based smoothed finite element method (NS-FEM) for upper bound solution to visco-elastoplastic analysis of solids using triangular and tetrahedral meshes," *Computer Methods in Applied Mechanics and Engineering*, vol. 199, no. 45–48, pp. 3005–3027, 2010.
- [21] G. R. Liu, T. Nguyen-Thoi, and K. Y. Lam, "An edge-based smoothed finite element method (ES-FEM) for static, free and forced vibration analyses of solids," *Journal of Sound and Vibration*, vol. 320, no. 4-5, pp. 1100–1130, 2009.
- [22] Z. C. He, G. Y. Li, Z. H. Zhong et al., "An edge-based smoothed tetrahedron finite element method (ES-T-FEM) for 3D static and dynamic problems," *Computational Mechanics*, vol. 52, no. 1, pp. 221–236, 2012.
- [23] T. T. Nguyen, G. R. Liu, K. Y. Lam et al., "A face-based smoothed finite element method (FS-FEM) for 3D linear and geometrically non-linear solid mechanics problems using 4-node tetrahedral elements," *International Journal for Numerical Methods in Engineering*, vol. 78, no. 3, pp. 324–353, 2009.
- [24] G. R. Liu, T. Nguyen-Thoi, and K. Y. Lam, "A novel alpha finite element method (α FEM) for exact solution to mechanics problems using triangular and tetrahedral elements," *Computer Methods in Applied Mechanics and Engineering*, vol. 197, no. 45–48, pp. 3883–3897, 2008.
- [25] W. Zeng, G. R. Liu, D. Li, and X. W. Dong, "A smoothing technique based beta finite element method (β FEM) for crystal plasticity modeling," *Computers and Structures*, vol. 162, pp. 48–67, 2016.
- [26] Y. Dong, G. W. Meng, and L. M. Zhou, "An inhomogeneous Cell-based smoothed finite element method for free vibration calculation of functionally graded magnetoelastoelectroelastic structures," *Shock and Vibration*, vol. 2018, Article ID 5141060, 17 pages, 2018.
- [27] M. Zaccariotto, T. Mudric, D. Tomasi, A. Shojaei, and U. Galvanetto, "Coupling of FEM meshes with Peridynamic grids," *Computer Methods in Applied Mechanics and Engineering*, vol. 330, pp. 471–497, 2018.
- [28] I. Babuška and J. M. Melenk, "Partition of unity method," *International Journal for Numerical Methods in Engineering*, vol. 40, pp. 727–758, 1997.
- [29] J. M. Melenk and I. Babuška, "The partition of unity finite element method: basic theory and applications," *Computer Methods in Applied Mechanics and Engineering*, vol. 139, no. 1–4, pp. 289–314, 1996.
- [30] J. T. Oden, C. A. M. Duarte, and O. C. Zienkiewicz, "A new cloud-based hp finite element method," *Computer Methods in Applied Mechanics and Engineering*, vol. 153, no. 1-2, pp. 117–126, 1998.
- [31] T. Strouboulis, I. Babuška, and K. Copps, "The design and analysis of the generalized finite element method," *Computer Methods in Applied Mechanics and Engineering*, vol. 181, no. 1–3, pp. 43–69, 2000.
- [32] M. A. Schweitzer, "Stable enrichment and local pre-conditioning in the particle-partition of unity method," *Numerische Mathematik*, vol. 118, no. 1, pp. 137–170, 2010.
- [33] Y. Cai, X. Zhuang, and H. Zhu, "A generalized and efficient method for finite cover generation in the numerical manifold method," *International Journal of Computational Methods*, vol. 10, no. 5, article 1350028, 2013.
- [34] T. Belytschko, R. Gracie, and G. Ventura, "A review of extended/generalized finite element methods for material modeling," *Modelling and Simulation in Materials Science and Engineering*, vol. 17, no. 4, article 043001, 2009.
- [35] S. Y. Jiang and C. B. Du, "Coupled finite volume methods and extended finite element methods for the dynamic crack propagation modelling with the pressurized crack surface," *Shock and Vibration*, vol. 2017, Article ID 3751340, 16 pages, 2017.
- [36] J. P. Xu and S. Rajendran, "A "FE-Meshfree" TRIA3 element based on partition of unity for linear and geometry nonlinear analyses," *Computational Mechanics*, vol. 51, no. 6, pp. 843–864, 2012.
- [37] R. Tian, G. Yagawa, and H. Terasaka, "Linear dependence problems of partition of unity-based generalized FEMs," *Computer Methods in Applied Mechanics and Engineering*, vol. 195, no. 37-40, pp. 4768–4782, 2006.
- [38] S. Rajendran and B. R. Zhang, "A "FE-meshfree" QUAD4 element based on partition of unity," *Computer Methods in Applied Mechanics and Engineering*, vol. 197, no. 1–4, pp. 128–147, 2007.
- [39] S. Rajendran and B. R. Zhang, "Corrigendum to "A "FE-meshfree" QUAD4 element based on partition of unity," *Computer Methods in Applied Mechanics and Engineering*, vol. 197, no. 13–16, p. 1430, 2008.
- [40] X.-h. Tang, C. Zheng, S.-c. Wu, and J.-h. Zhang, "A novel four-node quadrilateral element with continuous nodal stress," *Applied Mathematics and Mechanics*, vol. 30, no. 12, pp. 1519–1532, 2009.
- [41] Y. Zhang, X. Tang, and H. Zheng, "A three-node triangular element with continuous nodal stress," *Computers and Structures*, vol. 141, pp. 46–58, 2014.
- [42] Y. Yang, L. Chen, X. Tang, H. Zheng, and Q. Liu, "A partition-of-unity based "FE-Meshfree" hexahedral element with continuous nodal stress," *Computers and Structures*, vol. 178, pp. 17–28, 2017.
- [43] J. P. Xu and S. Rajendran, "A partition-of-unity based "FE-Meshfree" QUAD4 element with radial-polynomial basis functions for static analyses," *Computer Methods in Applied Mechanics and Engineering*, vol. 200, no. 47-48, pp. 3309–3323, 2011.
- [44] Y. Yang, R. Bi, and H. Zheng, "A hybrid "FE-Meshless" QUAD4 with continuous nodal stress using radial-polynomial basis functions," *Engineering Analysis with Boundary Elements*, vol. 53, pp. 73–85, 2015.
- [45] Y. Yang, D. Xu, and H. Zheng, "A partition-of-unity based "FE-Meshfree" triangular element with radial-polynomial basis functions for static and free vibration analysis," *Engineering Analysis with Boundary Elements*, vol. 65, pp. 18–38, 2016.
- [46] Y. Cai, X. Zhuang, and C. Augarde, "A new partition of unity finite element free from the linear dependence problem and possessing the delta property," *Computer Methods in Applied*

- Mechanics and Engineering*, vol. 199, no. 17–20, pp. 1036–1043, 2010.
- [47] Y. Yang, X. Tang, and H. Zheng, “Construct “FE-Meshfree” Quad4 using mean value coordinates,” *Engineering Analysis with Boundary Elements*, vol. 59, pp. 78–88, 2015.
- [48] Y. Yang, D. Xu, and H. Zheng, “Application of the three-node triangular element with continuous nodal stress for free vibration analysis,” *Computers and Structures*, vol. 169, pp. 69–80, 2016.
- [49] B. R. Zhang and S. Rajendran, ““FE-Meshfree” QUAD4 element for free-vibration analysis,” *Computer Methods in Applied Mechanics and Engineering*, vol. 197, no. 45–48, pp. 3595–3604, 2008.
- [50] Y. Yang, L. Chen, D. Xu, and H. Zheng, “Free and forced vibration analyses using the four-node quadrilateral element with continuous nodal stress,” *Engineering Analysis with Boundary Elements*, vol. 70, pp. 1–11, 2016.
- [51] S. Zheng, B. R. Zhang, and K. M. Liew, “A partition of unity-based “FE-Meshfree” QUAD4 element for geometric nonlinear analysis,” *International Journal for Numerical Methods in Engineering*, vol. 82, no. 12, pp. 1574–1608, 2010.
- [52] Y. Yang, G. Sun, and H. Zheng, “Application of the “FE-Meshfree” QUAD4 with continuous nodal stress using radial-polynomial basis functions for vibration and geometric nonlinear analyses,” *Engineering Analysis with Boundary Elements*, vol. 78, pp. 31–48, 2017.
- [53] L. Yao, W. Tian, L. Li, and L. Yao, “Numerical investigations of a partition-of-unity based “FE-Meshfree” QUAD4 element with radial-polynomial basis functions for acoustic problems,” *Applied Mathematical Modelling*, vol. 40, no. 13, pp. 6199–6217, 2016.
- [54] M. A. Yao, C. S. Chen, and H. Bowman, “Some recent results and proposals for the use of radial basis functions in the BEM,” *Engineering Analysis with Boundary Elements*, vol. 23, no. 4, pp. 285–296, 1999.
- [55] V. N. V. Do and C. H. Lee, “Nonlinear analyses of FGM plates in bending by using modified radial point interpolation mesh-free method,” *Applied Mathematical Modelling*, vol. 57, pp. 1–20, 2018.
- [56] F. Liu and J. Zhao, “Upper bound limit analysis using radial point interpolation meshless method and nonlinear programming,” *International Journal of Mechanical Sciences*, vol. 70, no. 70, pp. 26–38, 2013.
- [57] J. Chung and G. M. Hulbert, “A time integration algorithm for structural dynamics with improved numerical dissipation: the generalized- α method,” *Journal of Applied Mechanics*, vol. 60, no. 2, pp. 371–375, 1993.
- [58] K.-J. Bathe, “Conserving energy and momentum in nonlinear dynamics: a simple implicit time integration scheme,” *Computers and Structures*, vol. 85, no. 7-8, pp. 437–445, 2007.
- [59] K.-J. Bathe and G. Noh, “Insight into an implicit time integration scheme for structural dynamics,” *Computers and Structures*, vol. 98-99, no. 5, pp. 1–6, 2012.
- [60] G. Noh and K.-J. Bathe, “Further insights into an implicit time integration scheme for structural dynamics,” *Computers and Structures*, vol. 202, pp. 15–24, 2018.
- [61] B. Boroomand, M. Najjar, and E. Oñate, “The generalized finite point method,” *Computational Mechanics*, vol. 44, no. 2, pp. 173–190, 2009.
- [62] A. Shojaei, U. Galvanetto, T. Rabczuk, A. Jenabi, and M. Zaccariotto, “A generalized finite difference method based on the Peridynamic differential operator for the solution of problems in bounded and unbounded domains,” *Computer Methods in Applied Mechanics and Engineering*, vol. 343, pp. 100–126, 2019.
- [63] S. P. Timoshenko and J. N. Goodier, *Theory of Elasticity*, McGraw-Hill Book Company, New York, NY, USA, 3rd edition, 1970.
- [64] C. A. Brebbia, J. C. F. Telles, and L. C. Wrobel, *Boundary Element Techniques*, Springer-Verlag, Berlin, Germany, 1984.

